SSCL-323

SSCL-323

Superconducting Super Collider Laboratory

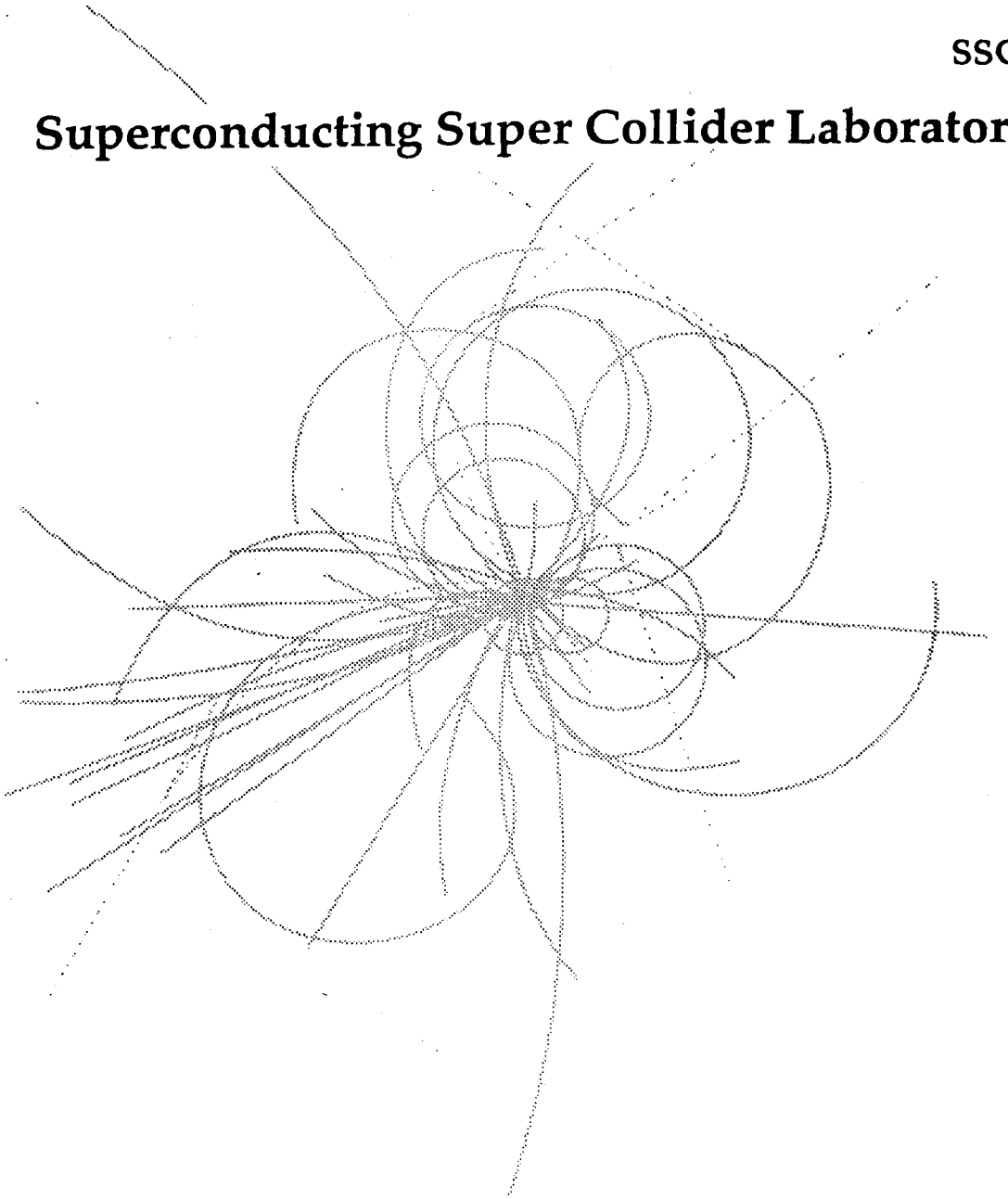

Tune Modulation and E778 Experiment

T. Chen

May 1990

SSCL-323

TUNE MODULATION AND E778 EXPERIMENT

Tong Chen

Accelerator Division
Superconducting Super Collider Laboratory*
2550 Beckleymeade Avenue
Dallas, Texas 75237

May 1990

*Operated by the Universities Research Association, Inc., for the U.S. Department of Energy under Contract No. DE–AC02–89ER40486.

SSCL-323

Tune Modulation and E778 Experiment

Tong Chen

Abstract

Tune modulation effect on nonlinear beam dynamics is studied. Different tune modulation conditions will lead to different motion properties. Boundaries on modulation condition are found to distinguish qualitatively different motions. The motion in resonance island with tune modulation is modeled by a driven pendulum. Its nonlinear property is analyzed, and investigated by simulation. Experiments have been done to observe the phenomena predicted by the theory. Many interesting results provide evidence for it.

1.0 INTRODUCTION

This note reports the recent progress of a part of E778 experiment, which is a nonlinear beam dynamics experiment performed in the Fermilab Tevatron. This experiment was motivated by the desire to reduce uncertainties in the design of the Superconducting Super Collider (SSC), and to determine if the nonlinear effects are predictable from calculation. Observations were made which are applicable to areas of physics much broader than accelerator physics.

For this experiment, the Tevatron can be regarded as a linear system. Controlled nonlinear elements, 16 strong sextupole magnets, added in the Tevatron, created the nonlinear environment anticipated in the SSC. The basic experimental procedure starts with a "needle beam;" the size of the beam was reduced by a collimator. Then, a pulsed kicker is fired to induce coherent betatron oscillation. The displacement of the centroid of the beam is picked up and recorded by two sets of beam position monitor. These measurements are used to generate phase space plots, or other analysis.

Up to now, E778 has had three runs, in May 1987, February 1988, and June 1989. Experiments included of smear-tune shift measurement, injection experiment, dynamic aperture measurement, resonance island-tune modulation experiment, and two-degree-of-freedom resonance experiment. This note describes the resonance island-tune modulation experiment. New theory is developed, and interesting agreement with experiments is shown. Applicable fields reach beyond accelerator physics.

This note only describes what has been done in this part of the experiment. The purpose is to provide a document for later experiments. Any discussion and comments are welcome.

2.0 TUNE MODULATION THEORY

Tune modulation has an important role in nonlinear beam dynamics because it is related to many problems such as resonance, chaotic motion, dynamic aperture, and decay mechanism. As a part of the E778 experiment, tune modulation was investigated theoretically and experimentally. Theoretical study shows that tune modulation could be represented as a simple driven pendulum, or a Josephson Junction. In other words, it is a general nonlinear problem.

2.1 Five Unperturbed Islands—The Single Resonance Hamiltonian, H_5

First, it is necessary to develop a vocabulary for the one dimensional motion near the 2/5 resonance which is observed in E778. The convenient action angle variables, (J,ϕ), are related to the horizontal displacement and angle, (X, X'), *at a fixed point*, by

$$\begin{pmatrix} (2J)^{1/2}\sin(\phi) \\ (2J)^{1/2}\cos(\phi) \end{pmatrix} = \begin{pmatrix} \frac{1}{\sqrt{\beta(s)}} & 0 \\ \frac{\alpha}{\sqrt{\beta}} & \sqrt{\beta} \end{pmatrix} \begin{pmatrix} X \\ X' \end{pmatrix}, \qquad [1]$$

where α and β are Twiss parameters. That is, J behaves much like the betatron amplitude, while ϕ is the betatron phase of a trajectory under study. If the base tune Q_0 is close to 2/5, motion is well approximated by the the *single resonance Hamiltonian :*

$$H_5 = 2\pi (Q_0 - \tfrac{2}{5}) J + V_{40}J^2 - V_{55} J^{5/2} \cos(5\phi + \phi_5). \qquad [2]$$

This is just shorthand for the five-turn difference equations of motion:

$$\begin{pmatrix} J \\ \phi \end{pmatrix}_{t+5} = \begin{pmatrix} J \\ \phi \end{pmatrix}_t + 5 \begin{pmatrix} -\dfrac{\partial H_5}{\partial \phi} \\ \dfrac{\partial H_5}{\partial J} \end{pmatrix}_t, \qquad [3]$$

demonstrating that t is an integer divisible by five.

The meaning of the three terms in H_5 becomes clear when the partial differentiations in Equation [3] are performed. The first term leads to a small constant net phase advance of $10\pi (Q_0 - 2/5)$, but the second term causes an advance of $10\, V_{40}J$, linearly proportional to the action. That is, the amplitude dependent tune is

$$Q(J) = Q_0 + \left(\frac{V40}{p}\right) J, \qquad [4]$$

consistent with the experimentally observed variation:

$$Q = Q_0 - 7 \times 10^{-4}\, a^2 \qquad [5]$$

when Q_0 π 0.42, and the amplitude a is in millimeters. The resonance action J_I is found by solving Equation [4] with $Q(J_I) = 2/5$. It is now convenient to rewrite H_5 as an expansion around J_I:

$$H_5 = \frac{1}{2} U I^2 - V \cos(5\phi), \qquad [6]$$

where

$$I = J - J_I, \quad U = 2\, V_{40}, \quad V = V_{55} J_I^{5/2}, \qquad [7]$$

and the value of ϕ_5 has been arbitrarily set to zero.

Substitution of Equation [6] into Equation [3] (with J replaced by I) shows that $(I,\phi) = (0,0)$ is a fixed point—a trajectory launched there is stationary. In a region close enough to $I = 0$, then, H_5 may be considered as representing differential equations of

motion, continuous in t, which agree well with the difference motion whenever t divides by five. In this approximation,

$$\begin{pmatrix} \frac{dI}{dt} \\ \frac{d\phi}{dt} \end{pmatrix} = \begin{pmatrix} -\frac{\partial H_5}{\partial \phi} \\ \frac{\partial H_5}{\partial I} \end{pmatrix} = \begin{pmatrix} -5V\sin(5\phi) \\ U\ I \end{pmatrix} \qquad [8]$$

or, in terms of a single second order equation of motion,

$$\frac{d^2\phi}{dt^2} + 5\,VU\sin(5\phi) = 0, \qquad [9]$$

which is equivalent to the equation of a free pendulum. The small amplitude motion is

$$\begin{pmatrix} I \\ \phi \end{pmatrix} = \phi_0 \begin{pmatrix} 5\left(\frac{V}{U}\right)^{1/2}\sin(2\pi Q_I t) \\ \cos(2\pi Q_I t) \end{pmatrix} \qquad [10]$$

where the *island tune* Q_I is given by

$$Q_I = \frac{5}{2\pi}(U\,V)^{1/2}. \qquad [11]$$

Figure 1 shows the presence of five resonance islands (in normalized X,X′ space) under simulated E778 experimental conditions.

The apparently continuous sequence of dots which follow a single trajectory in Figure 1 are represented in the theory by contours of H_5, which describe a parabolic valley along the I-axis, modulated along the ϕ-axis by the $\cos(5\phi)$ term. This leads to five local minima separated by five saddle points, corresponding to five stable and five unstable fixed points. The island half-width is found by equating the saddle point elevation with the elevation at $\phi = 0$:

$$I_W = 2\left(\frac{V}{U}\right)^{1/2}. \qquad [12]$$

2.2 The Island Tune, Q_I

According to the previous simplified theory, a nonlinear resonance is determined by principle parameters—U and V. They come from multipole terms and their cross terms. In principle, they can be calculated by high-order perturbation theory, but, as we know, it is difficult to get useful results from higher order perturbation theory. Also, the effects from other resonances are hard to calculate. In order to test and improve the theory, some measurements are planned in E778.

The island tune Q_I and island width I_W are important parameters of resonance. They can be derived from U and V directly, and they are measurable. By measuring these parameters, the agreement among the measurements can be checked with theoretical

knowledge. U is the detuning term; it can be found through the measurement of the detuning function Q(a). The island width I_W is related to the fraction of particles captured on the resonance islands. Because Q_I is a frequency signal, the measurement of Q_I is supposed to be easier and more accurate.

Unfortunately, the Q_I signal is not easily found in experimental data. When a single particle is captured close to the center of an island, a Fourier transform of its amplitude or phase reveals a peak at Q_I. This has been proved by simulation. In the real experiment, one cannot do a single particle launching; a bunch of particles will occupy a part or the total area of the island and its surrounding area, so that the signal becomes quite complicated. Because the island tune depends on the particle amplitude from the center of the island, the multi-particle effect blurs the Q_I peak.

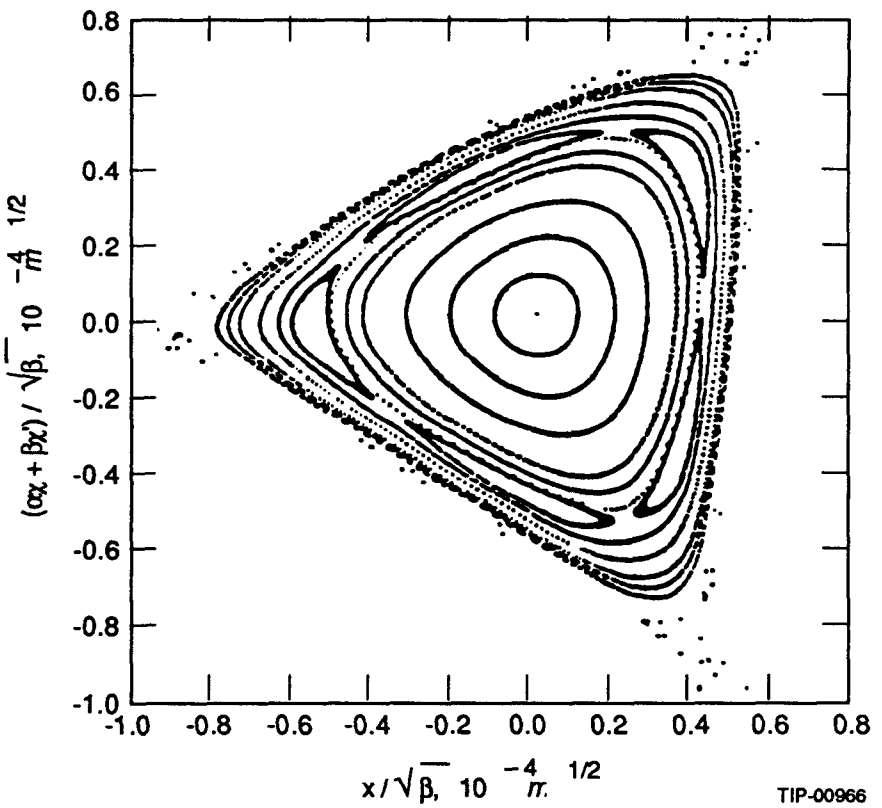

Figure 1. Poincaré Plot Generated by Numerically Tracking Particles of Various Amplitudes.

A test program was written to investigate the frequency domain situation of a signal with many frequencies. This program, called *fakeisl*, generates ideal phase-modulated signal with damping:

$$\phi = 2\pi\,(\,\psi + q_{res}\,t\,), \qquad [13]$$

where $\psi = \exp(-\frac{t^2}{2\tau^2})\,A_\phi \sin 2\pi Q_I t$ and [14]

q_{res} is the resonance tune (e.g., $q_{res} = 2/5$) .

Then the amplitude is calculated as

$$a = \sqrt{2(I_r + I_W \cos \phi)} \quad . \qquad [15]$$

The data outputs simulate position signals from two BPMs:

$$x1 = a \cos(f\text{-}f1)$$

$$x_2 = a \cos(\phi + \phi_2). \qquad [16]$$

The output format is compatible with TEVEX, so that the data can be analyzed by TEVEX. Figure 2 shows the signal and spectrum from TEVEX. Even the damping term makes the peak broader, the peak is still clear.

The multi-frequency case, like the real situation in a resonance island, was introduced by taking the sum of position signals with different island amplitudes and frequencies. For example,

$$QI, j = QI0(j/10)$$

$$AW, j = AW0(1.1 - j/10)$$

$$j = 1, 2, ..., 10$$

so that the Q_I will vary from $0.1Q_{I0}$ to Q_{I0}, and A_W will vary from A_{W0} to $0.1A_{W0}$. The output "signals" are the sum

$$x_1 = \Sigma\, x_{1,j}$$

$$x_2 = \Sigma\, x_{2,j}.$$

As the result, the Q_I peak becomes ambiguous (Figure 3). This is similar to tracking results shown in Figure 4. The conclusion is that the effect of particles with different tunes will give a flat spectrum, even though the signal in the time-domain has a visible wave. Actually, the spectrum will fall down at Q_I, as shown in the pictures. The edge should provide the information of Q_I. Unfortunately, a clear edge has never been found in experimental data so far. According to the author's experience in simulation, the following improvements should be made to look for the edge in experiment. Increase the capture fraction by reducing beam emittance, and/or choose a sextupole configuration which provides a larger island size. In addition, one should reduce noise from the environment and other electronic modules.

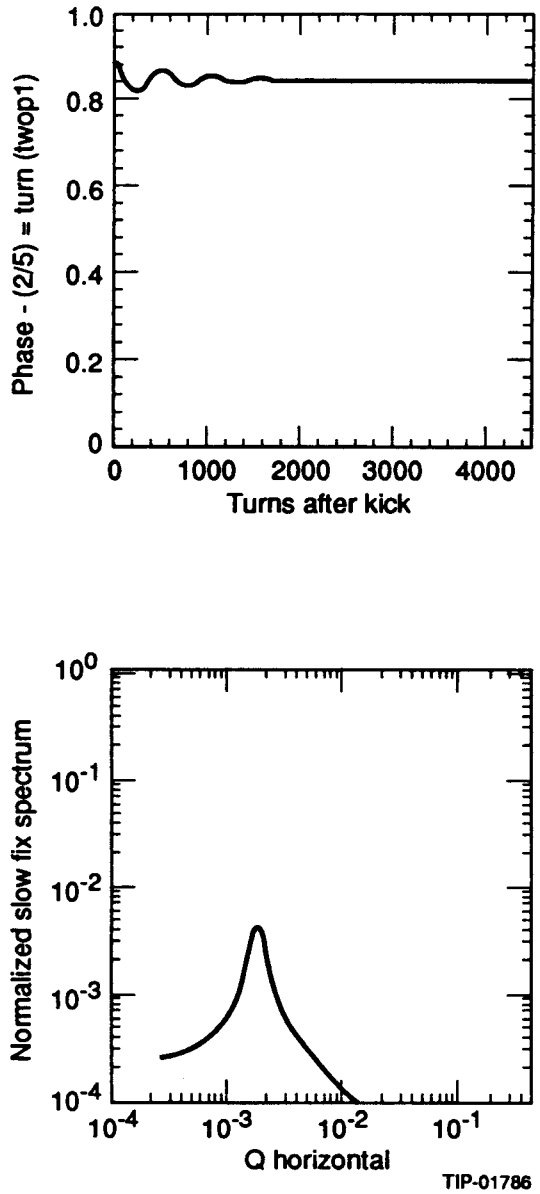

Figure 2. Spectrum of a Damping Oscillation.

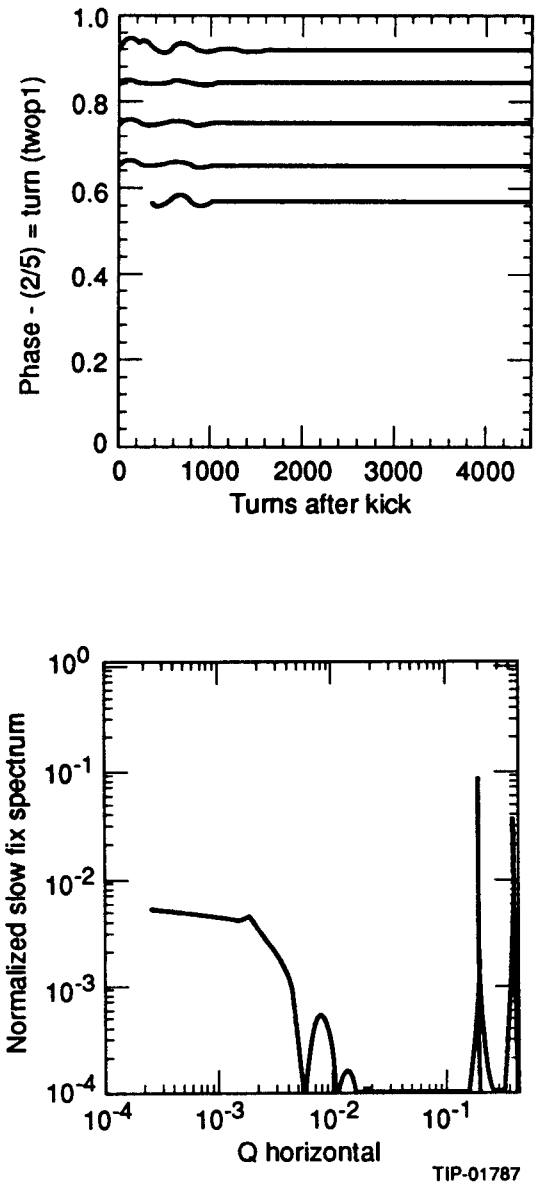

Figure 3. Spectrum of Sum of Many Different Frequency Oscillations.

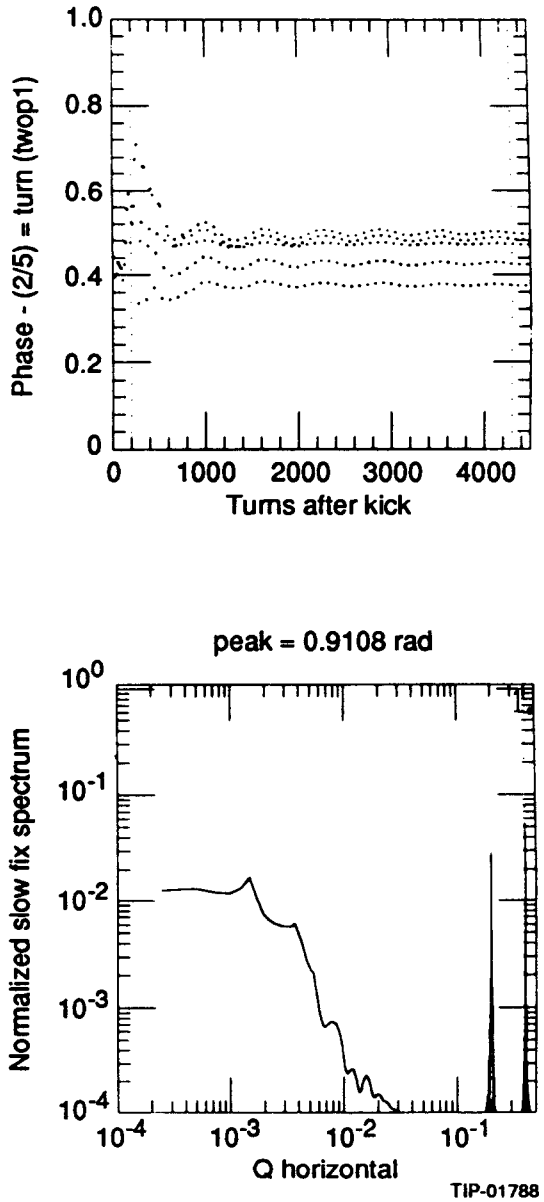

Figure 4. Spectrum of EVOL Multi-particles Tracking.

2.3 Five Islands With Tune Modulation

If a set of quadrupoles is perturbed by a small sinusoidal current, the base tune is modulated according to

$$Q_0 = Q_{00} + q \sin(2\pi Q_M t), \qquad [17]$$

where q and Q_M are the tune modulation amplitude and tune. Tune modulation is included in the resonance Hamiltonian by adding a single term to Equation [6], giving

$$H_5 = 2\pi q \sin(2\pi Q_M t) I + \frac{1}{2} U I^2 - V \cos(5\phi). \qquad [18]$$

Now H_5 is time-dependent, so it is no longer conserved, and it is no longer possible to picture the motion by plotting its contours. The two first order equations of motion are

$$\begin{pmatrix} \frac{dI}{dt} \\ \frac{d\phi}{dt} \end{pmatrix} = \begin{pmatrix} -5V \sin(5\phi) \\ 2\pi q \sin(2\pi Q_M t) + UI \end{pmatrix}, \qquad [19]$$

while the single second order differential equation in f,

$$\frac{d^2\phi}{dt^2} + (2\pi Q_I)^2 \frac{\sin(5\phi)}{5} = (2\pi)^2 q Q_M \cos(2\pi Q_M t) \qquad [20]$$

is explicitly analogous to the driven pendulum equation

$$\frac{d^2\theta}{dt^2} + (2\pi Q_I)^2 \sin(\theta) = D \cos(2\pi Q_M t), \qquad [21]$$

with 5ϕ replacing θ. There is a family of possible solutions periodic in Q_M:

$$5\phi = k\, 2\pi (Q_M t) + \sum_{n=1}^{\infty} c_n \cos(n\, 2\pi Q_M t). \qquad [22]$$

The tune of the k-th solution

$$Q_k = \frac{2}{5} + \frac{1}{2\pi} \left\langle \frac{d\phi}{dt} \right\rangle = \frac{2}{5} + k \frac{Q_M}{5} \qquad [23]$$

demonstrates the possibility of a family of stable sidebands. Each sideband has five islands, at an action I_k given by $Q(I_k) = Q_k$, so $I_k = k \frac{2\pi Q_M}{5\, U}$. [24]

If solution k is stable, then persistent signals should be observed at Q_k when a beam is kicked on top of one of the sideband islands.

The small angle approximation can be made on Equation [20]:

$$\frac{d^2\phi}{dt^2} + (2\pi Q_I)^2\phi = (2\pi)^2 q Q_M \cos(2\pi Q_M t). \qquad [25]$$

The solution is illuminating. It is given, for all Q_M, by

$$\phi = \frac{Q_M^2}{Q_I^2 - Q_M^2} \frac{q}{Q_M} \cos(2\pi Q_M t) \qquad [26]$$

$$I = \frac{Q_I^2}{Q_I^2 - Q_M^2} \frac{2\pi q}{U} \sin(2\pi Q_M t). \qquad [27]$$

At constant q, the action amplitude goes to $(2\pi q)/U$ for small Q_M, while the phase amplitude goes to zero. So we call the slow modulation region "amplitude modulation." The action amplitude goes to zero, but the phase amplitude goes to q/Q_M for large Q_M, so that the fast modulation is called "phase modulation."

This is valid only for the case of small angle oscillation; that is, far away from $Q_M = Q_I$ resonance. Here we define the small angle condition as $5\Phi < 1$, where Φ is the amplitude of ϕ. Because $\sin(5\phi)$ is approximated to 5ϕ when Equation [20] becomes Equation [25], $\sin(5\phi)$ must be smaller than 1. From Equation [26], we get the small angle condition

$$\left|\frac{qQ_M}{Q_I^2 - Q_M^2}\right| = \frac{1}{5}. \qquad [28]$$

Other approximations can be applied to explain the mechanism.

If the tune changes adiabatically, it is reasonable to approximate the rate of change as constant, at its global maximum. The Hamiltonian in Equation [18] then becomes

$$H_5 = (2\pi)^2 q Q_M t\, I + \frac{1}{2} U I^2 - V\cos(5\phi), \qquad [29]$$

which corresponds to a pendulum with constant torque. This is still time-dependent, but now a canonical transformation is possible from (I,ϕ,H_5) to $(\bar{I},\bar{\phi},\bar{H}_5)$, making $\bar{H}_5$ time-independent. Specifically, the generating function

$$F_3(I,\bar{\phi},t) = -I\bar{\phi} - \varepsilon t\bar{\phi} - \frac{1}{6}\varepsilon^2 t^3, \qquad [30]$$

where $\varepsilon = \dfrac{(2\pi)^2 qQ_M}{U} = 25\,V\dfrac{q\,Q_M}{Q_I^2}$,

gives, by its definition Equation [6],

$$\bar{I} \equiv -\frac{\partial F_3}{\partial \bar{\phi}} = I + \varepsilon t, \qquad \phi \equiv -\frac{\partial F_3}{\partial I} = \bar{\phi} \tag{31}$$

$$\bar{H}_5 \equiv H_5 + \frac{\partial F_3}{\partial t} = \frac{1}{2} U\bar{I}^2 - V\cos(5\bar{\phi}) - \varepsilon\,\bar{\phi}. \tag{32}$$

While the old and new phases are identical, the new action drifts relative to the old action at a constant speed. The $\varepsilon\phi$ term in the new Hamiltonian has serious consequences for the stability of the $k = 0$ fundamental island chain. Pictorially, this non-periodic term corresponds to a constant slope along the quadratic Hamiltonian valley. If this slope is steep enough, there are no longer any local minima. There are no stable islands at all if $|\varepsilon| > 5V$, that is, if

$$\frac{qQ_M}{Q_I^2} > \frac{1}{5}\,. \tag{33}$$

In the slow limit, this corresponds to the small angle boundary in Equation [28] .

We now consider the case where tune modulation occurs rapidly, i.e., $Q_M >> Q_I$. In this region, a time-independent Hamiltonian is found by first applying the generating function

$$F_3(I,\bar{\phi},t) = -I\bar{\phi} - \frac{q}{Q_M}\cos(2\pi Q_M t)\, I, \tag{34}$$

which gives

$$\bar{H}_5 = \frac{1}{2} U\bar{I}^2 - V\cos(5\bar{\phi} + \frac{5q}{Q_M}\cos(2\pi Q_M t)) \tag{35}$$

$$= \frac{1}{2} U\bar{I}^2 - V\sum_i J_i\left(\frac{5q}{Q_M}\right)\cos(5\bar{\phi} + i\,2\pi Q_M t),$$

where the J_i are integer-order Bessel functions. The Hamiltonian is made time-independent by concentrating on the vicinity of the k-th sideband, near the action I_k, and averaging the sum in Equation [35] over one modulation period, to give

$$H_{5k} = \frac{1}{2} U\,(I - I_k)^2 - V\,J_k\left(\frac{5q}{Q_M}\right)\cos(5\phi) \tag{36}$$

(without overbars, and with a shift of origin). This differs from the simple form in Equation [6] by the J_k factor, which determines whether the k-th sideband is significant. As a rule of thumb, $J_k(A) \approx 0$ i $|A| < |k|$, so sideband k is significant if

$$q > |k|\frac{Q_M}{5}\,. \tag{37}$$

The right-hand side of Equation [37] is the separation of the sideband tune from the fundamental resonance tune, corresponding to the sensible physical condition that says, for the resonance to be felt near an action I_k, the tune must be modulated far enough to cross the fundamental.

The sidebands are isolated from each other if their separation in action, given by [23], is larger than the sideband width, given by [12] with $J_k V$ replacing V. Chaos appears if the sidebands overlap, spanning the action range of sidebands of significant size. It is easily shown by further approximating J_k, that sideband overlap is expected if [37] is true, and if

$$Q_M^{3/4} (5\,q)^{1/4} < \frac{4}{\pi^{1/4}} Q_I \qquad [38]$$

Because of the casual Bessel function approximation, sidebands overlap a little earlier or later than this semi-quantitative condition suggests.

Figure 5 shows the four dynamical phases in the (q,Q_M) parameter space. The solid line with the pole in the figure,

$$\left|\frac{qQ_M}{Q_I^2 - Q_M^2}\right| = \frac{1}{5}$$

is the small angle boundary below which Equation [26] applies. Rigorous analysis (below) shows that this is the stability boundary for the $k = 0$ solution in the slow modulation limit. Rigorous analysis in the large Q_M limit shows that, although the $k \neq 0$ sideband islands are stable, their size is insignificant below the small angle boundary. The other boundary is the nearly vertical solid line in Figure 5, which is based on Equation [36]. Roughly speaking, on the right-hand side of the boundary there appear multi-sidebands. On the left-hand side, the chaotic region appears because of the overlapping of sidebands.

2.4 Iteration

It is necessary to rely on numerical iterative and simulation solutions when $Q_M \approx Q_I$ From Equation [20], an iteration formula can be established:

$$\frac{d^2\phi_{new}}{dt^2} + \omega_I^2\,\phi_{new} = \omega_I^2\left(\phi_{old} - \frac{\sin(5\phi_{old})}{5}\right) + B\cos(2\pi\,Q_M\,t), \qquad [39]$$

where $\omega_I = 2\pi\,Q_I$, $B = (2\pi)^2\,qQ_M$. Substituting Equation [22] into Equation [39], the left-hand side becomes:

$$\text{left side} = (\omega_I^2 - (n\,2\pi\,Q_M)^2) \sum_{n=1}^{\infty} c_{n\,new} \cos(n\,2\pi\,Q_M t). \qquad [40]$$

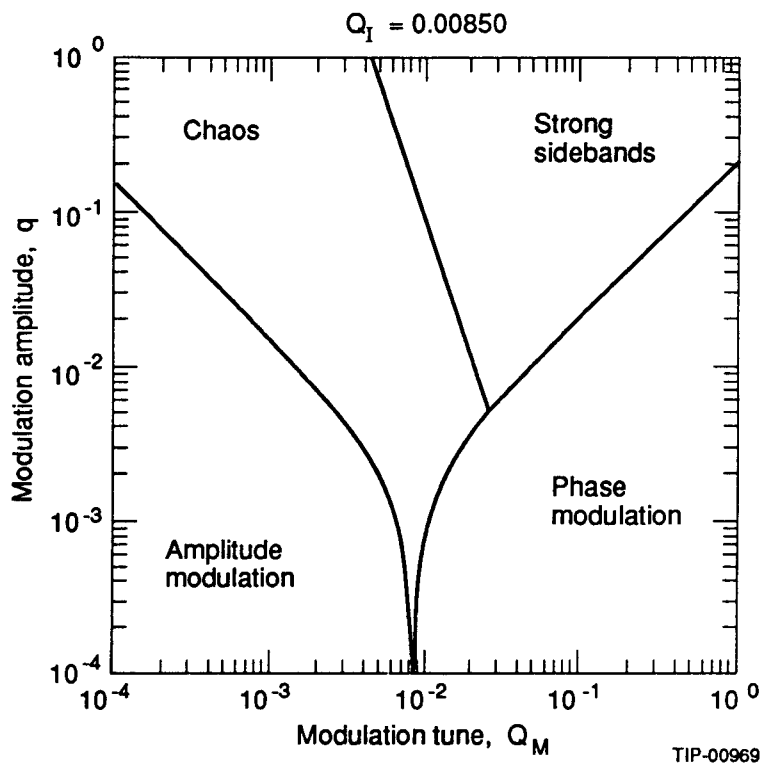

Figure 5. The Dynamical Phases in E-Qm Space.

If one does an FFT on the right-hand side expression, one gets a Fourier expansion:

$$\sum_{n=1}^{\infty} c_{n\,old} \cos(n\, 2\pi\, Q_M t). \qquad [41]$$

For iteration, put Equation [40] equal to Equation [41], so that

$$c_{n\,new} = \frac{1}{\omega_I^2 - (n\, 2\pi\, Q_M)^2}\, c_{n\,old}. \qquad [42]$$

An iteration program, *iter*, was written based on the previous formula. The number of terms expanded in FFT can be 32 to 128. The solution's stability is checked by the program. For the $k = 0$ case, the boundary of stable solution agrees with the boundary defined by Equation [28] for $Q_M < Q_I$ (Figure 6). On the other side, $Q_M > Q_I$, the solution is stable everywhere. When $k \neq 0$, all solutions are unstable for $Q_M < Q_I + \varepsilon$, where ε is a small number, and depends on k. Above $Q_I + \varepsilon$, all solutions are stable.

2.5 Simulation

Simulation was done using the tracking code EVOL. A single particle is launched into the center of the islands, and then the motion in phase space is observed. It is easy to distinguish the stable island case from chaotic motion, so that the boundary can be found.

Figure 7 shows the result. In the region of Q_M close to Q_I, simulation and the prediction by Equation [26] agree well.

When Q_M is far away from Q_I, the small angle solution, Equations [26–28], can be used. The phase motion consists of two parts: one is its normal phase advance, the other is the phase modulation, which could take the form of the solution of Equation [26]. The phase motion can be expressed as

$$\phi = 2\pi\, Q_0 t + \phi \cos(2\pi\, Q_M t). \qquad [43]$$

The related particle position is

$$x = (a_0 + \delta\hat{a} \cos(2\pi Q_M t)) \cos(\, 2\pi\, Q_0 t + \phi \cos(2\pi\, Q_M t) + \phi_0\,). \qquad [44]$$

By applying Bessel function identities, x comes out like

$$x = \sum_{k=-\infty}^{\infty} (a_0 + k\delta\hat{a}/\phi)\, J_k(\, \phi\,) \cos(\, 2\pi\, (Q_0 + kQ_M)t + \phi_0\,). \qquad [45]$$

The amplitude oscillation can be derived from the action motion of Equation [27] with $\delta\hat{a} = \frac{q}{Q_0'} \frac{QI2}{QI2 - QM2}$, where $Q_0' = \frac{dQ}{da}$ can be found by tracking. So, Equation [45] becomes

$$x = \sum_{k=-\infty}^{\infty} (a_0 + \frac{kQ_I^2}{Q_0'\, Q_M})\, J_k(\frac{qQ_M}{Q_I^2 - Q_M^2})\cos(\, 2\pi\, (Q_0 + kQ_M)t + \phi_0\,). \qquad [46]$$

The $k = \pm 1$ sideband strengths can be extracted:

$$A\pm = \pm(\, a_0 \pm \frac{Q_I^2}{Q_0'\, Q_M})\, J_1(\frac{qQ_M}{Q_I^2 - Q_M^2}\, . \qquad [47]$$

Figure 8 shows the variation of sideband strength with Q_M. Simulations are done by EVOL; the data were analyzed by TEVEX. The results are shown in Figure 8; a very good agreement can be seen in this picture.

It is important to mention that the sidebands discussed here are totally different from the sidebands in the upper right region of Figure 6. The former is from signal processing, the frequency spaces between sidebands are $1/Q_M$. But the latter is a high-order nonlinear resonance phenomenon; its frequency spaces between sidebands are $1/NQ_M$, where N is the resonance order. For 2/5 resonance here, N = 5.

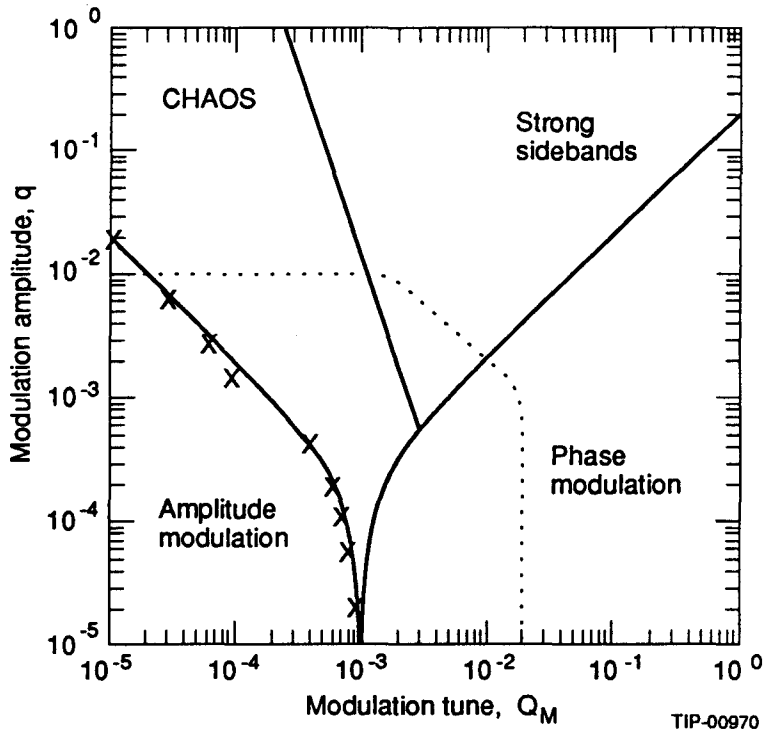

Figure 6. Iteration Agrees With the Chaotic Boundary for Qm<Qi.

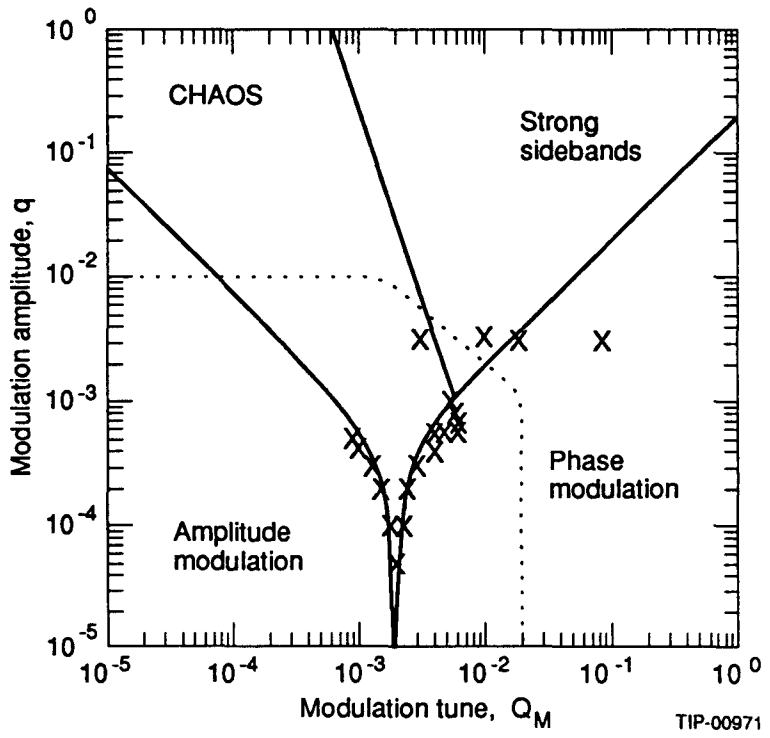

Figure 7. EVOL Tracking Results Which Verify the Chaos Dip.

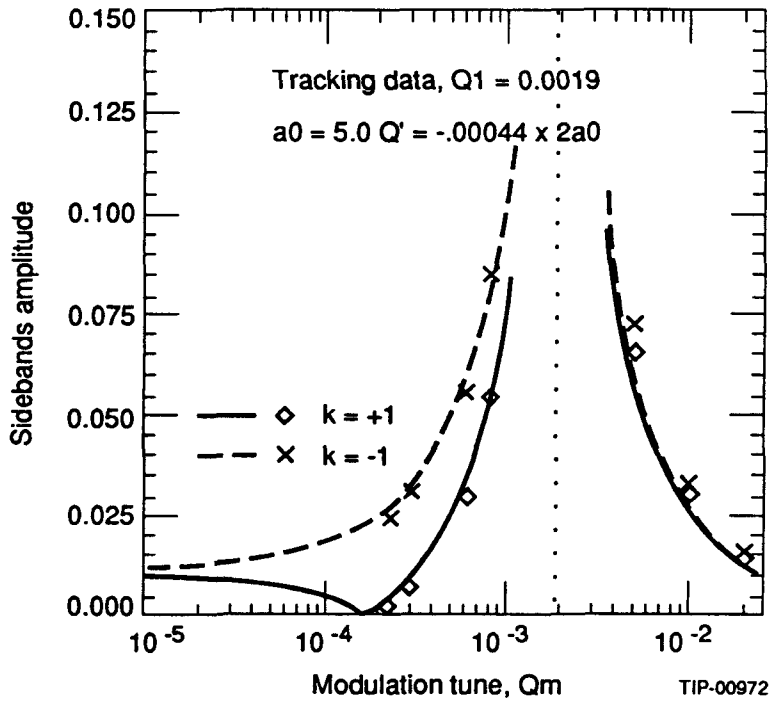

Figure 8. Modulation Sideband Strength Versus Qm. EVOL tracking results agree with theory calculation.

In principle, this is helpful in measuring Q_I. But the problem is that Equation [47] is only valid when the particle is launched at the center of islands, otherwise, the results can be much more complicated. More studies are needed on this subject.

Several pictures (Figures 9(a) through 9(f)) are created to explain what happens in the different phases of Figure 6. The simulation was done by EVOL. The tune was set close to the 1/6 resonance, and nonlinear sources are beam-beam interaction and sextupoles. Figure 9(a) shows the boundaries of different phases and tune modulation conditions for every simulation case with point 1-5 in (a) corresponding to Figures 9(b)-(f). Figure 9(b) is in the stable amplitude modulation region; six islands are clear. Figure 9(c) is obviously chaos. When Q_M becomes larger, some sidebands become stable and others become unstable. In Figure 9(d), a few sidebands appear among the chaotic motion. Figure 9(e) is in the multi-sidebands region, and many sidebands can be seen. In the phase modulation region, the stable fundamental islands appear again, the sidebands are suppressed. Chaotic motion does not exist any more (Figure 9(f)).

2.6 Mechanical Model

According to Equation [20], tune modulation can be easily modeled by a simple rigid gravity pendulum driven by a sinusoidal torque. It is helpful to understand the complicated tune modulation by considering the motion of a simple mechanical model.

Image that the pendulum has no free oscillation at the beginning, and that it is driven by a very slow torque. Because the pendulum's free oscillation frequency is much faster than the torque's frequency, the pendulum's response is fast enough to follow the

torque, so that the pendulum will move together with the applied torque. This is the case of amplitude modulation.

If the torque has a very fast frequency—much higher than the pendulum's free oscillation frequency—the pendulum will not be able to follow the torque in phase, but out of phase. From Equation [26], it is easy to see that the amplitude of ϕ motion $qQ_M/(Q_I^2 - Q_M^2)$ is positive when $Q_I > Q_M$, but it is negative when $Q_I < Q_M$; that means out of phase. This is similar to the "phase modulation."

In the case of very strong torque or when the torque's frequency is very close to the pendulum's free oscillation frequency, the amplitude of the pendulum's oscillation will be quite large; it may even turn around. This is a very nonlinear case, and the motion is very complicated. Because the pendulum's free oscillation frequency strongly depends on the amplitude of oscillation, it is hard to synchronize the motion of the pendulum and torque. The future motion of the pendulum depends not only on its position and momentum, but also on the torque's strength and direction. These conditions change with time without periodic regulation, so that the motion is chaotic. In some very special cases, periodic motion can reappear. For instance, if the initial condition of the pendulum is fast rotation, and if the torque's period happens to be nearly some integer number of turns of the rotation, the pendulum will continue its periodic motion. This is just the sideband case, and the number of turns completed in one modulation period corresponds to the sideband order number.

Besides mechanical model, an electronic model, Josephson Junction with an AC bias, has the same behavior. The understanding of tune modulation and driven pendulum could be very helpful to the research of Josephson Junction and general nonlinear dynamics.

It may be better to build a mechanical model pendulum to demonstrate the phenomena, because a simple mechanical model can be understood more easily. It was also proposed to build an electronic model by conventional electronic devices, and it will be convenient to observe the behavior under various conditions. The data taken from the electronic model can be compared with theory computation, and the boundaries can be verified.

2.7 Driven Pendulum and Digital Model

Since the driven pendulum is not only a model for tune modulation, but a general nonlinear problem as well, it is worth further study.

First of all, write down the equation of motion of a pure driven pendulum:

$$\frac{d^2\psi}{dt^2} + \omega_0^2 \sin\psi = \varepsilon \sin(\Omega t), \qquad [48]$$

where ω_0 is the frequency of small oscillation, Ω is the driven frequency, and ε is the amplitude of the driving torque. Those parameters are related to Q_I, Q_M and q in tune modulation. A program DPEND was written for simulation. This program integrates the pure driven pendulum equation and plots the result in phase space.

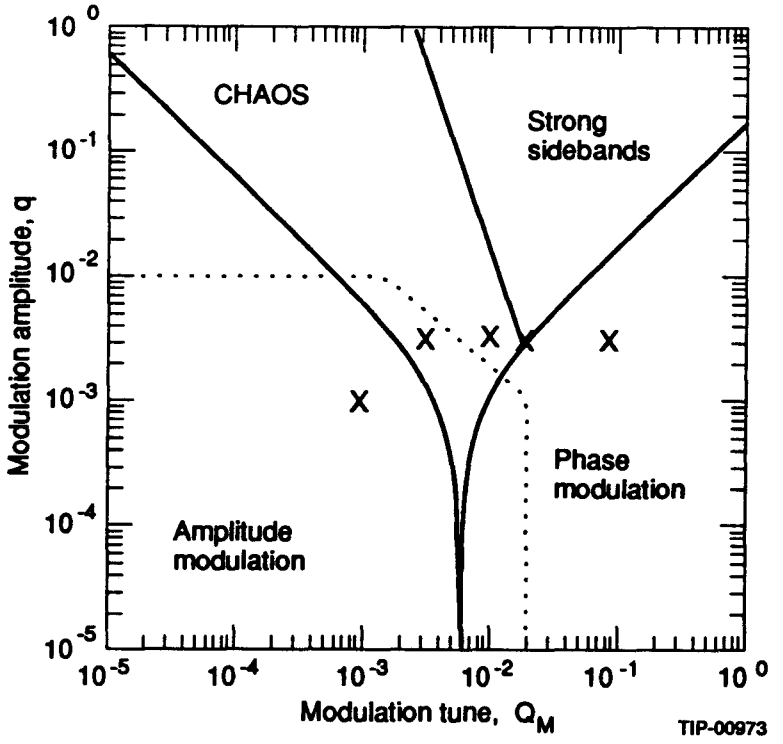

Figure 9(a). $Q_1 = 0.0061$, Resonance Order = 6

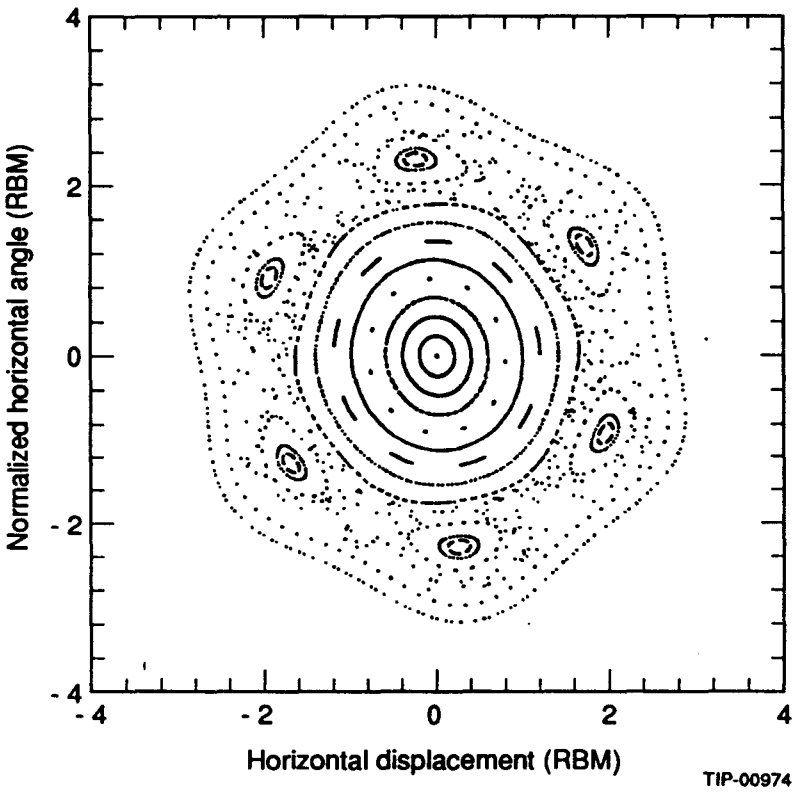

Figure 9(b).

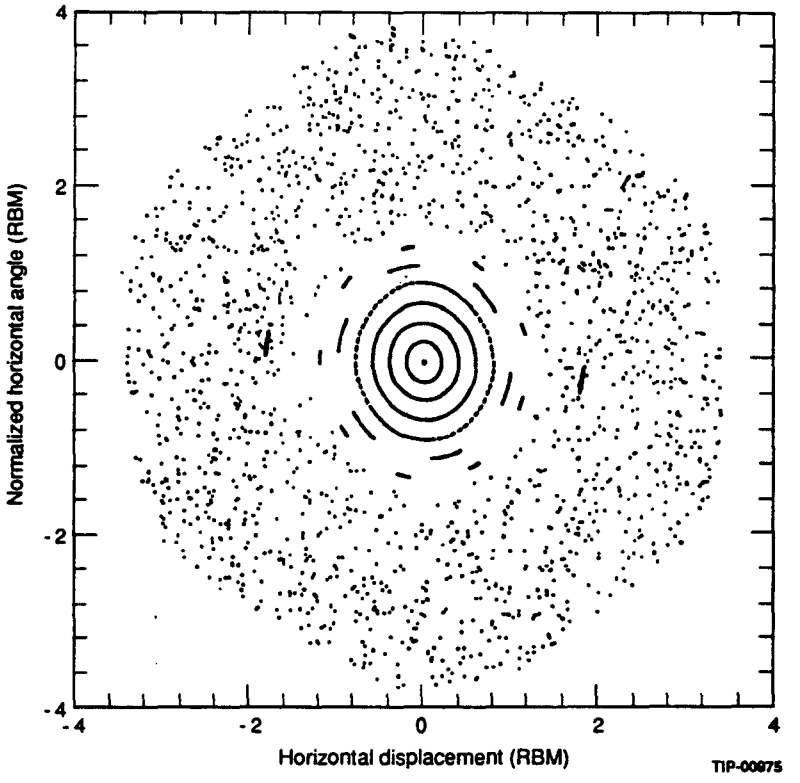

Figure 9(c).

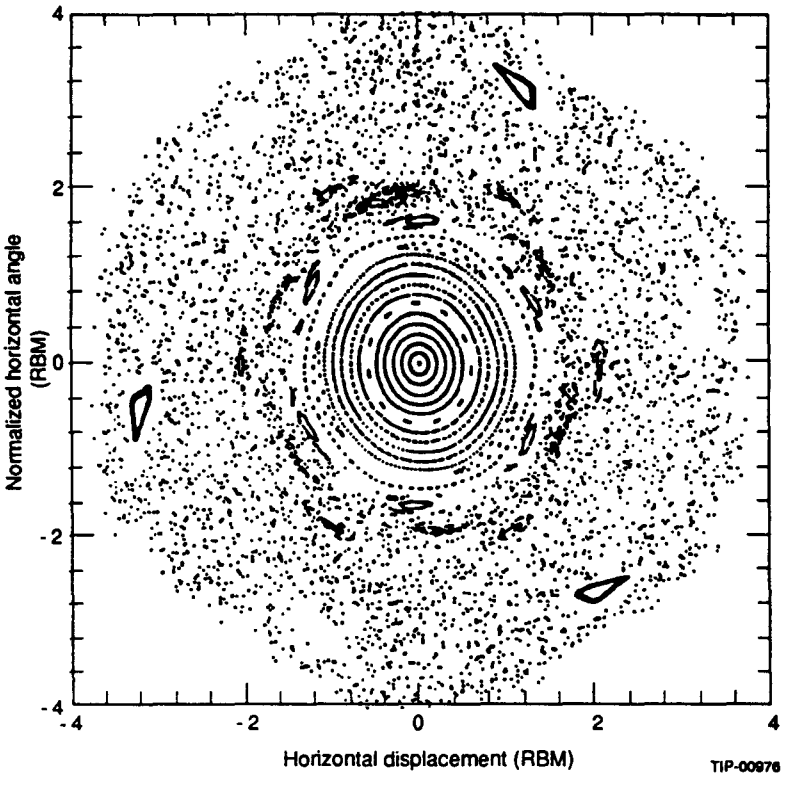

Figure 9(d).

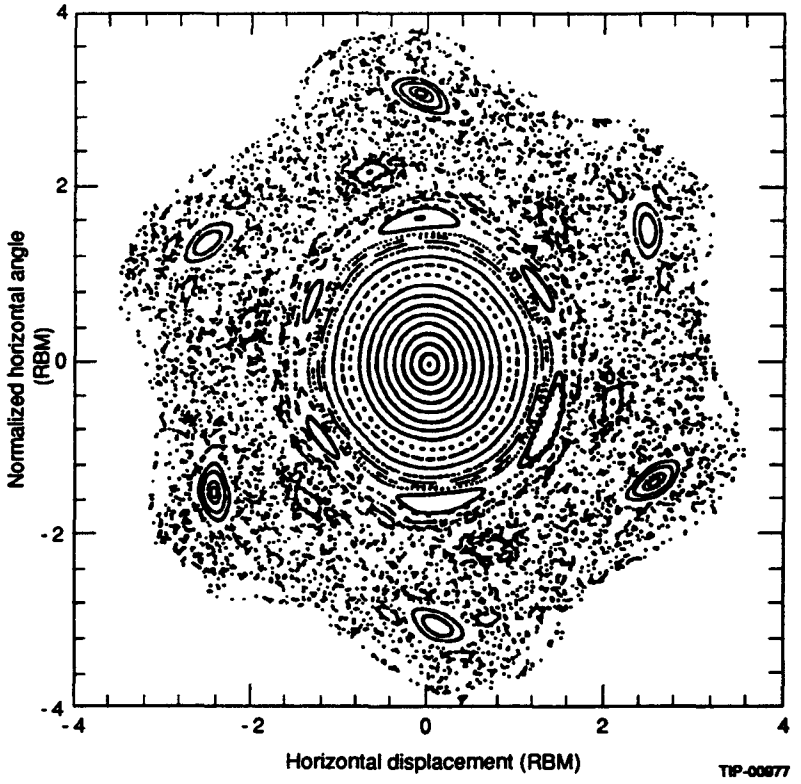

Figure 9(e).

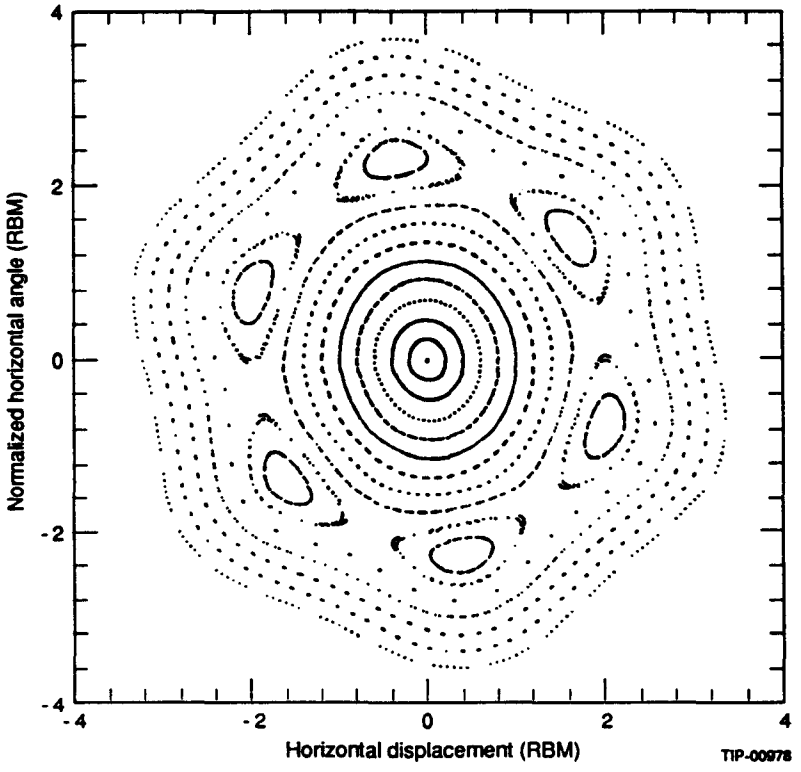

Figure 9(f).

The motion of a driven oscillator consists of free oscillation and driven motion. The driven motion part is more important because it dominates most properties of the motion. The following study will concentrate on driven motion only.

The driven motion is the motion with frequency identical to the driving frequency. To find a possible solution with this condition, assume the solution has the form of

$$\psi(t) = \alpha\sin(\Omega t). \qquad [49]$$

Substitute it into the equation of motion (Equation [48]), and use the identity

$$\sin[\alpha\sin(\Omega t)] = 2\sum_{k=0}^{\infty} J_{2k+1}(\alpha)\,\sin[(2k+1)\Omega t]. \qquad [50]$$

An equation of α is found:

$$-aW^2 + 2\,J_1(a)\,w_0^2 = \varepsilon. \qquad [51]$$

This equation can be solved by numerical method, but simplifying it by expending the Bessel Function to cubic term will be helpful to get a clearer idea. Under cubic approximation, Equation [51] becomes:

$$-aW^2 + aw_0^2\,[1-\frac{1}{8}a^2] = \varepsilon. \qquad [52]$$

According to our knowledge, this equation usually has three real solutions, but under some conditions, there are only one or two solutions. The solutions of the equation indicate where the island center is, this has been proved by a good agreement with simulation of DPEND for small α (Figure 10). In the simulation, the stable solution is the center of a stable island, and the unstable solution is a point where the solutions around it are divergence.

Notice that two stable solutions existed at the same time in the middle range. In this case, there are two stable islands, both of them $k = 0$ mode. Figures 11(a) through 11(e) are a series of simulation results with Q_M increasing. The upper island becomes weaker and weaker, then disappeared when Q_M increases, but lower island becomes stronger.

This fact introduces a new concept of driven oscillation. We knew that the amplitude of driven oscillation has a resonance peak at its free oscillation frequency, but it is suppressed when the driven frequency is far from its free oscillation frequency. Now we know that there are two different solutions for the driven motion, with driven frequency below and beyond free frequency oscillation frequency, respectively. One of the solutions is positive, the other is negative. This means that the driven motion is in phase or out of phase, comparing with driven force. It is comparable with the case of electrical oscillation circuit, which may be resistive, inductive, or capacitive.

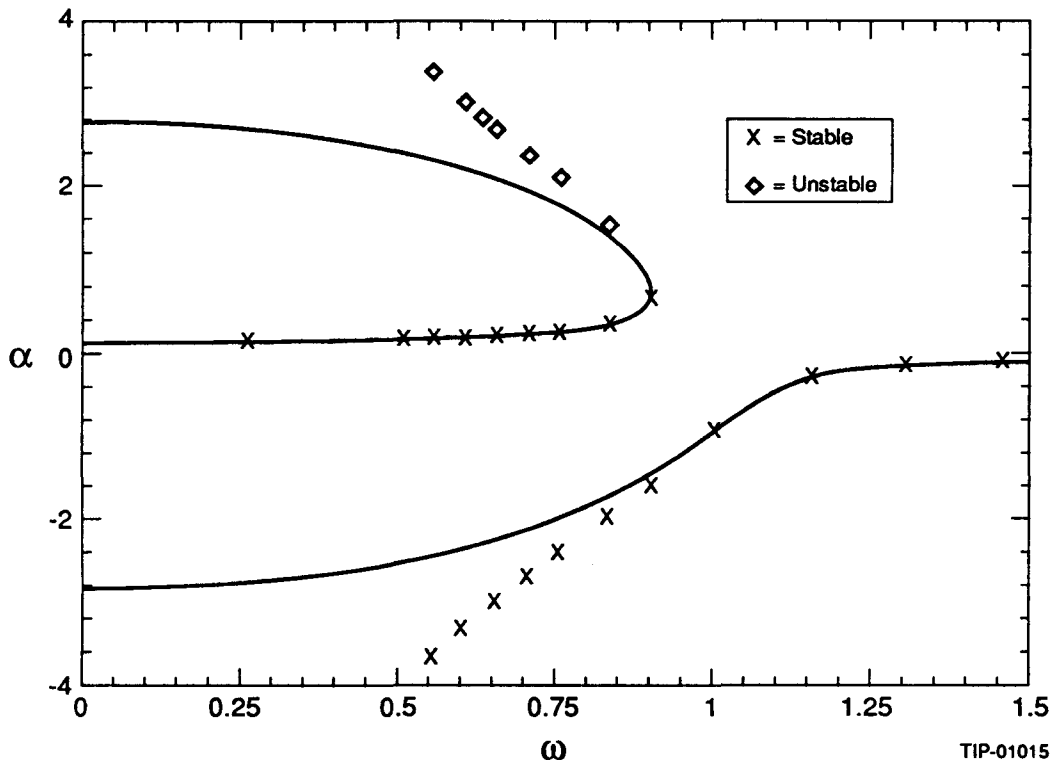

Figure 10. Solutions of α Changing With ω (= Ω /ωo) ε1 = 0.1.

It is easy to conclude that the boundary between chaotic motion and stable island should correspond to the condition where the two positive solutions meet. Simulation provides the answer. Figures 12(a) and 12(b) show the boundary points. In Figure 12(a), the simulation results agrees with the theoretical boundary very well. With the same data marked in Figure 12(b), some of them appear at the position where two positive roots meet. But for the case with large ε, or large q, this theory does not work. More study is needed for strong modulation.

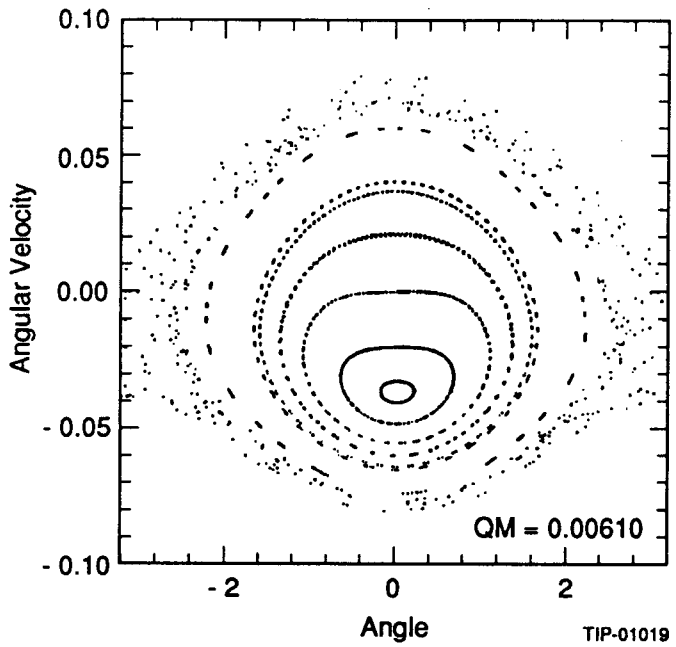

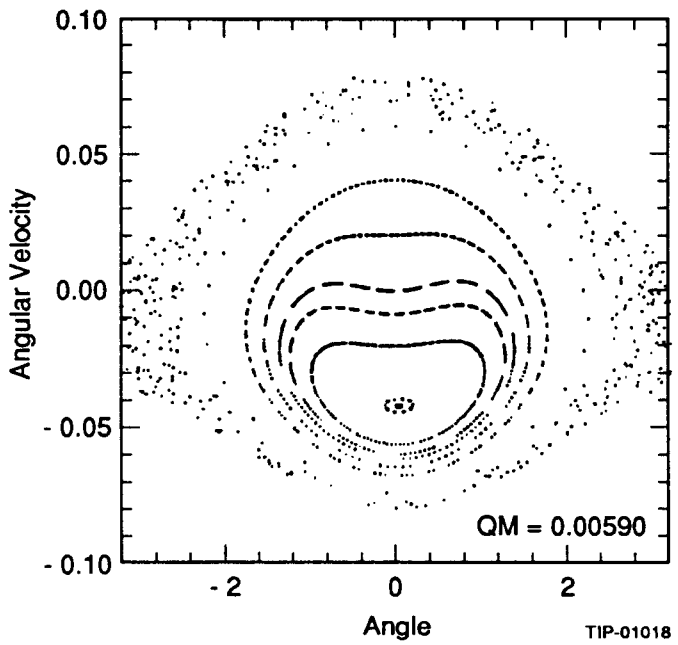

Figures 11(a) and 11(b). Phase Plot by DPEND.

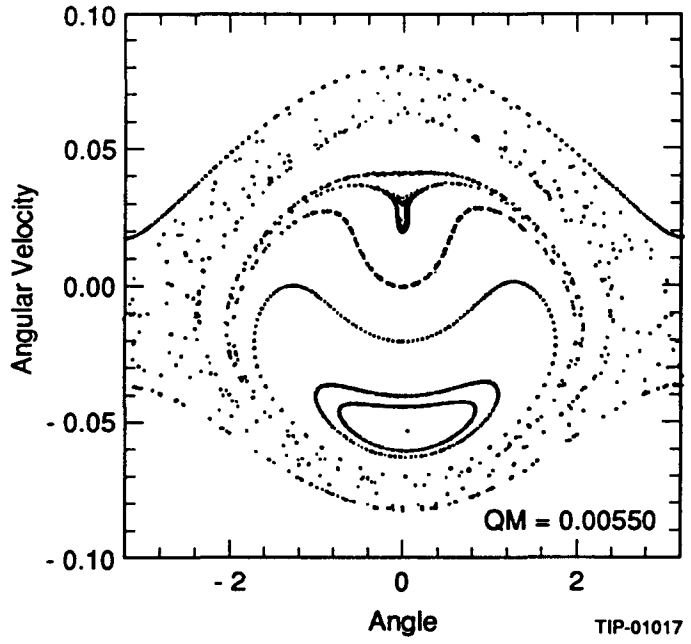

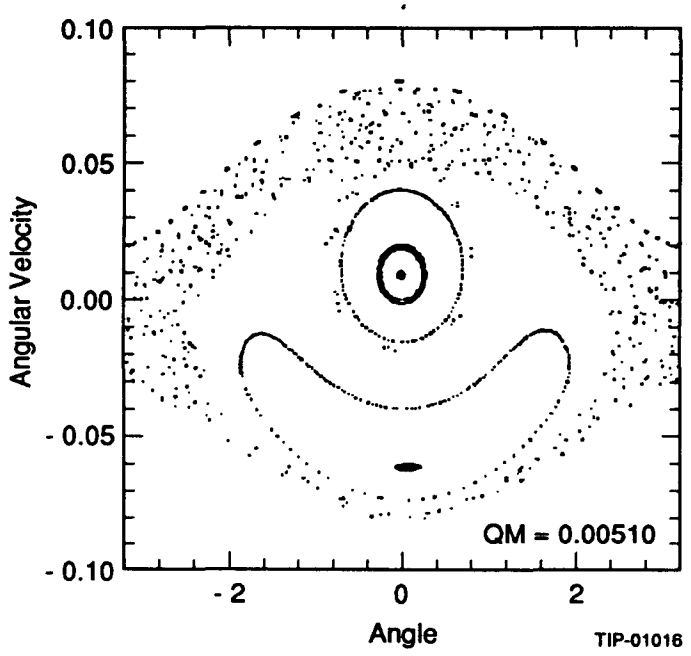

Figures 11(c) and 11(d).

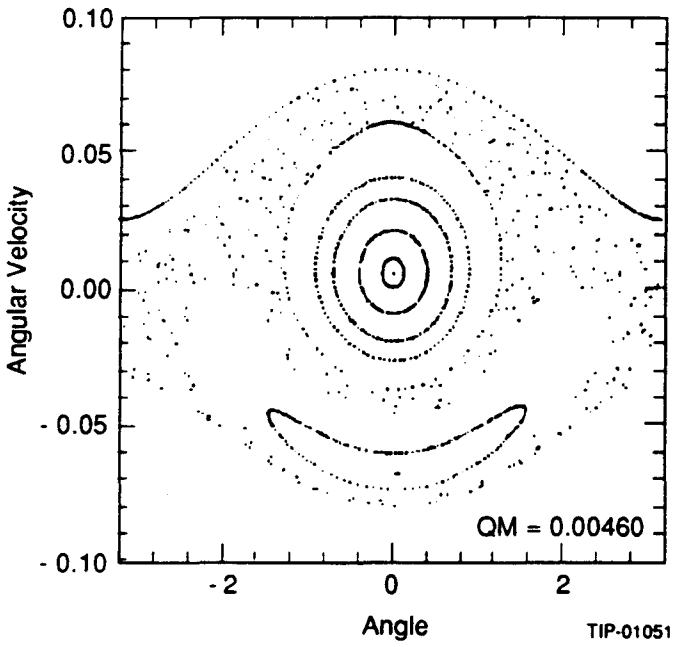
0.10
0.05
0.00
- 0.05
- 0.10
Angular Velocity
- 2
0
2
Angle
QM = 0.00460
TIP-01051

Figure 11(e).

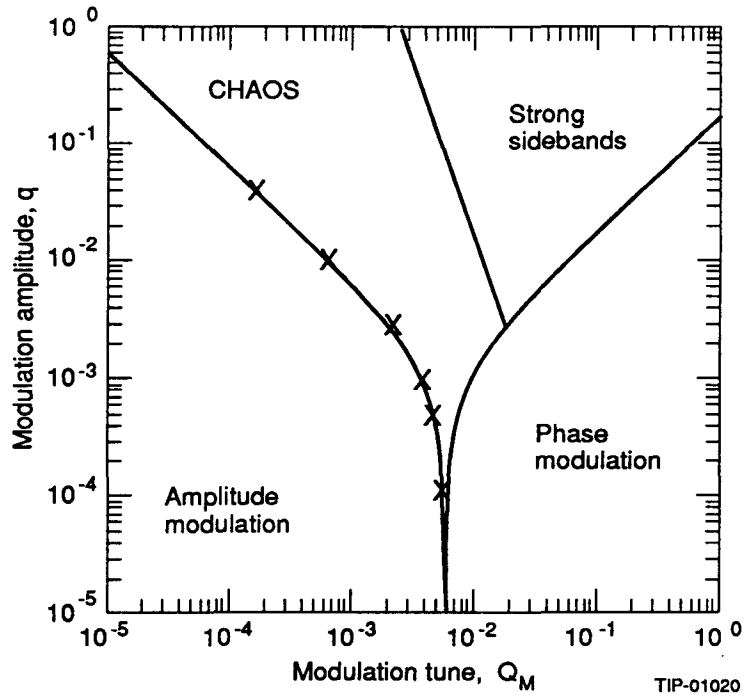

Figure 12(a). The Chaotic Boundary from DPEND Simulation Agrees With Theoretical One.

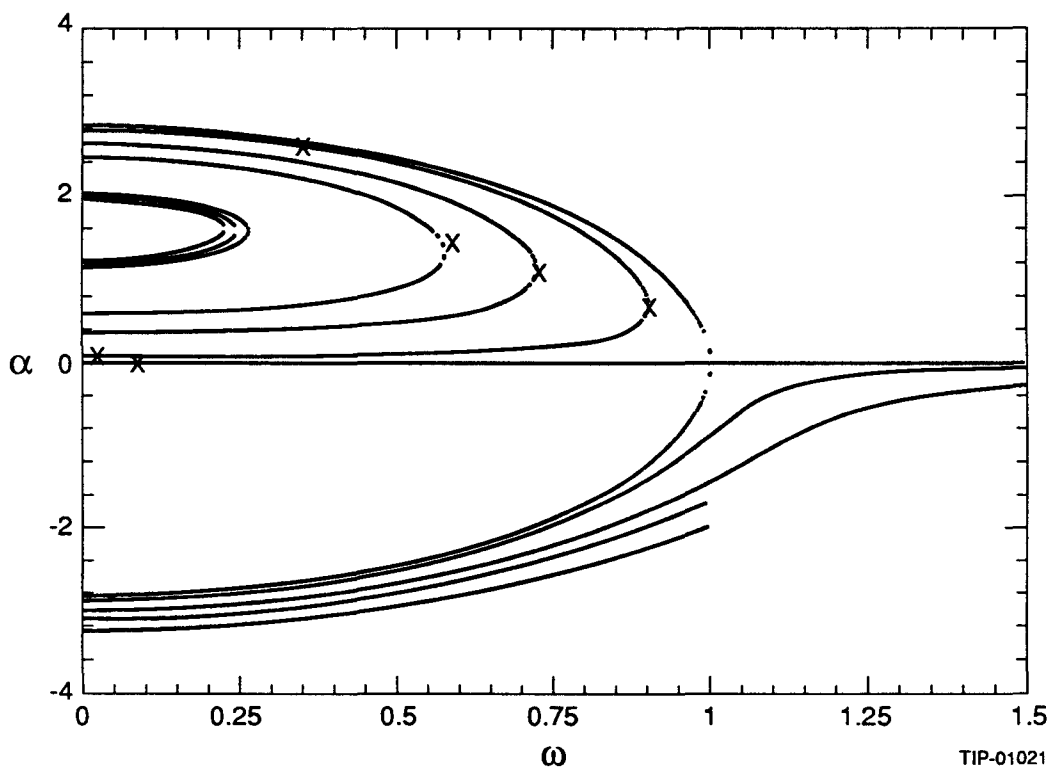

Figure 12(b). The Chaotic Boundary is Where the Stable and Unstable Solution of α Meet.

3.0 TUNE MODULATION EXPERIMENT

As a part of E778, the tune modulation experiment was carried out in a similar way. The nonlinear source is still the 16 special sextupoles located at F and C section. A collimator was used to reduce the beam size. The tune modulation was introduced by some quadrupoles excited by sinusoidal power supply. At the beginning of each shot, a kicker at E17 kicked the beam into a certain amplitude. Two horizontal BPMs (at F42 and F44) picked up the turn-by-turn signal, and the data acquisition system recorded them. The data would be read by computer. Some codes, like TEVEX and RESAN, were written for analyzing them, generating phase space plot, doing FFT, etc. The purposes of this experiment are to compare the results with theory, by observing sidebands, chaos motion, and their boundaries, and to measure Q_I.

The data was taken from the BPMs which are used in the other parts of the experiment; 64 K turns of data can be recorded per shot. Actually, two data sets were taken for each shot through different instruments. One is the original BPM resonance amplifier (CAMAC 5), the other is a newly developed peak-detector amplifier (CAMAC 9). The CAMAC 5, linear but noisy, is necessary for quantitative analysis. The CAMAC 9 is cleaner and more sensitive, but its output is nonlinear and hard to calibrate. CAMAC 9 data is helpful to observe weak sidebands in frequency domain.

The major tool used for analyzing data is RESAN. This program was developed with shared memory, so that it can load 64 kB data. The analysis is based on Fourier Transform. The time domain data are transformed into frequency domain period by period, and then the persistent signal strength can be measured versus time. The spectrums are arranged in a "mountain range" picture. One observe the frequency domain variation with time going on and looking for sidebands.

3.1 Results of the Experiment in February 1988

3.1.1 Persistent Signal Decay Rate and Chaos Boundaries

The persistent signal comes from the particles trapped in the 2/5 resonance islands. Its strength indicates how many particles are trapped in the islands. The persistent signal decay rate considers only the particular resonance signal decay after the decoherence period. It's a long time scale phenomenon. The decay rate is related to the stability of the islands. It is easy to imagine that there will be a large decay rate in the chaotic region because the islands are not stable there. Based on this idea, the decay rate was observed for finding the chaos boundary.

The persistent signal strength is related to the spectrum amplitude of the frequency which exactly presents the tune of 2/5. RESAN calculates the spectrum values periodically, and finds out its decay rate.

During the experiment, the 16 sextupoles are excited by 25 ampere current. Horizontal emittance was reduced by collimator to 2π (mm mrad). The horizontal basic tune was set to be 19.442 (which may be different from real value due to non-zero closed orbit at sextupoles). Three groups of data were taken with kicker voltage 9.5 kV, 8 kV, and 6.5 kV, respectively. In each group, tune modulation frequency and amplitude scan

the q–Q_M phase space, and data sets are recorded under different tune modulation conditions.

Figures 13(a) and 13(b) show the results with 9.5 kV kick. Figure 13(a) is the decay rate versus Q_M where a different symbol means different q. Their tune modulation conditions are plotted on Figure 13(b). In these scans, only the diamond scan rises rapidly; that is, this scan goes across the chaos boundary. By varying Q_I to fit the chaos boundary to where the decay rate begins to rise, Q_I is found to be 0.0085. Under this value, the experimental results can be explained very well. The scans with square and plus symbols stay inside the amplitude modulation and phase modulation region, respectively. Both of them are stable, so that they have low decay rates. The diamond scan goes through the boundary and gets into the chaos region, and the decay rate rises rapidly. A dramatic result is the cross (x) scan. Figure 13(b) shows that one data set is inside the chaos dip, and Figure 13(a) shows this data set has a much higher decay rate compared with the other data sets. This is a very good agreement, but, unfortunately, only one data set fell in this region. One could argue that this is an accidental data set.

Figures 14(a) and 14(b) give the 8 kV kicker voltage results. In this group, the scans with square and diamond symbols are just across the chaos boundary, and corresponding decay rates tend to rise. But the plus (+) scan is still inside the phase modulation stable region. None of them has a large decay rate.

Figures 15(a) and 15(b) show the 6.5 kV kicker voltage results. Unfortunately, no sets fell in the chaos region, so there is no rising decay rate.

In the previous analysis, Q_I has an uncertain value. It is adjusted to explain the experimental results. On the other hand, this provides a method to measure Q_I, even though it is not quite precise.

3.1.2 Modulation Sidebands

According to the theoretical analysis, there will be a sideband system caused by the phase and amplitude modulation. These sidebands will be spaced by the modulation frequency, and their strengths, if the particle sits in the island center, could be found by calculation. These sidebands clearly show up in the data analysis, and Figure 16 gives an example of the sidebands observed in data analysis. It is not clear how to compare the sideband strength with calculation because this is a multi-particle case. Only the sideband strength of the single particle sitting at the island center can be calculated and agrees with tracking result. For the multi-particle case, even the off-center single particle case, more work is necessary. But anyway, the experimental data show that the sideband strengths line up. Figures 17(a) and 17(b) show the result of the 9.5 kV kick data.

The lines in this picture are theoretical calculations from the single centered particle model. Q_I and Q' are adjusted to make the line fit the data. At the low modulation frequency region, changing Q_I means changing the slope of the lines, but changing Q' means changing their vertical position. For a better match between the data and calculation results, Q_I is taken as 0.012. This value may not make sense, and more understanding on the sideband strength is needed.

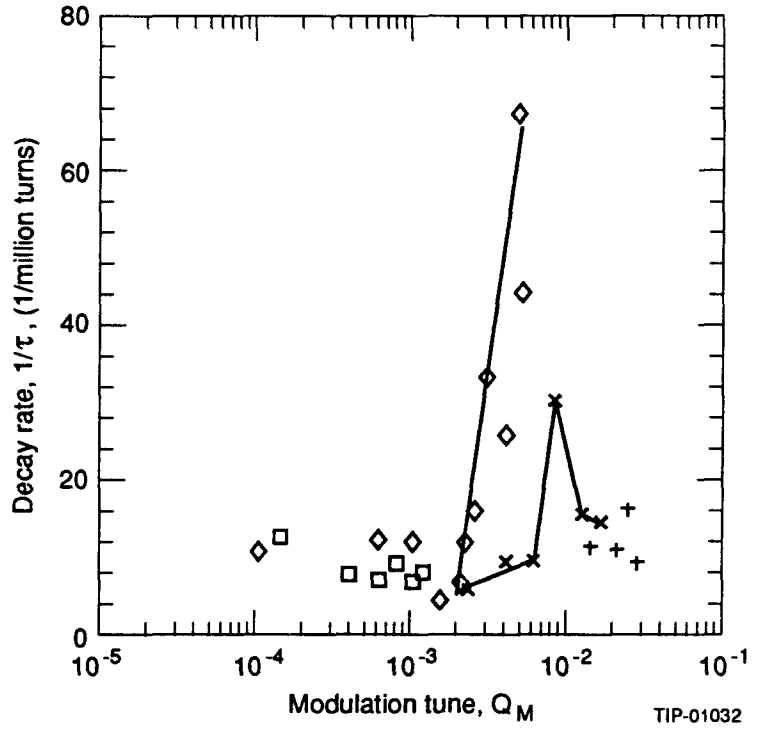

Figure 13(a). Persistent Signal Decay Rate Changing with 9.5kv Data.

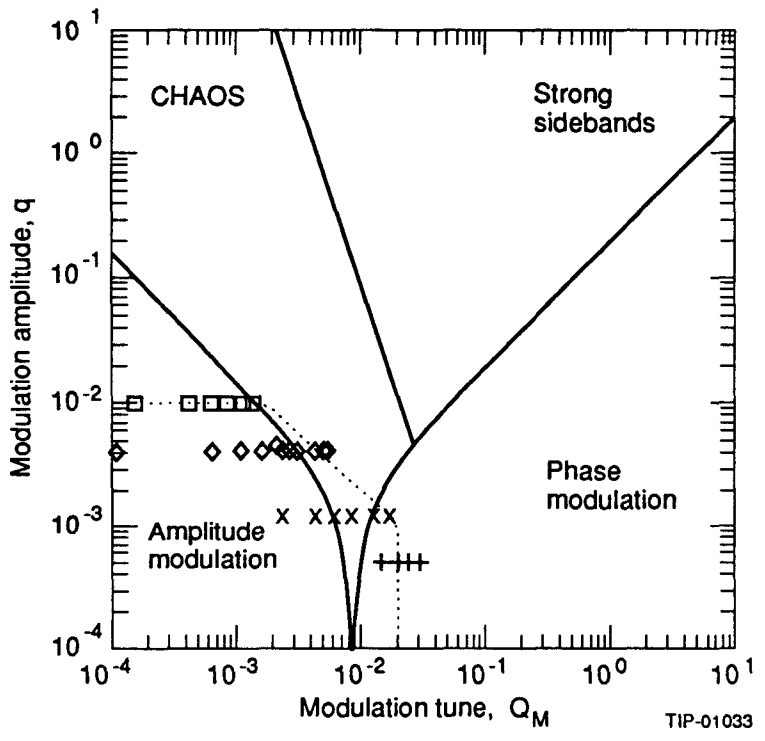

Figure 13(b). Tune Modulation Condition of the Data Shots Shown in (a).

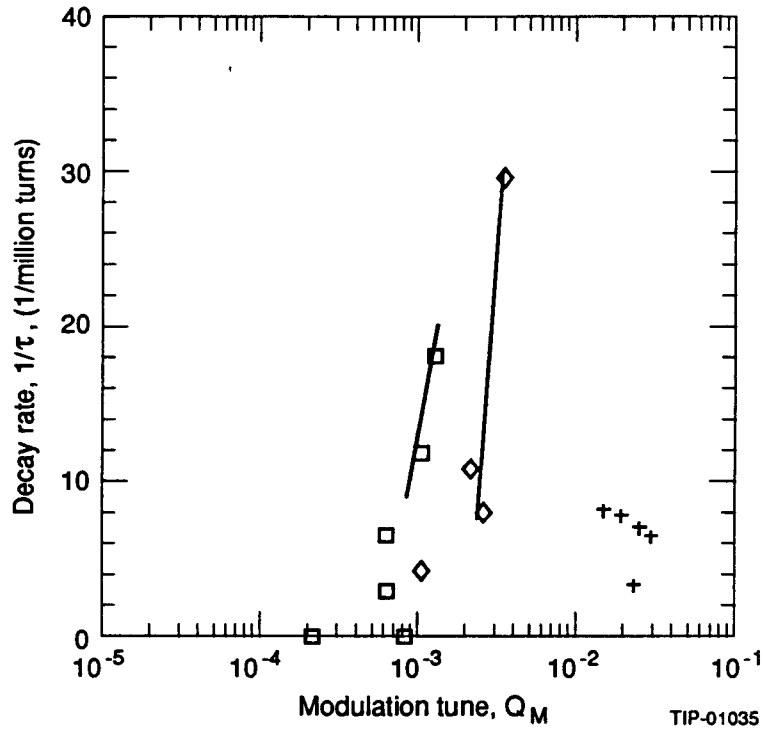

Figure 14(a). Persistent Signal Decay Rate Changing with Qm, 8kv Data.

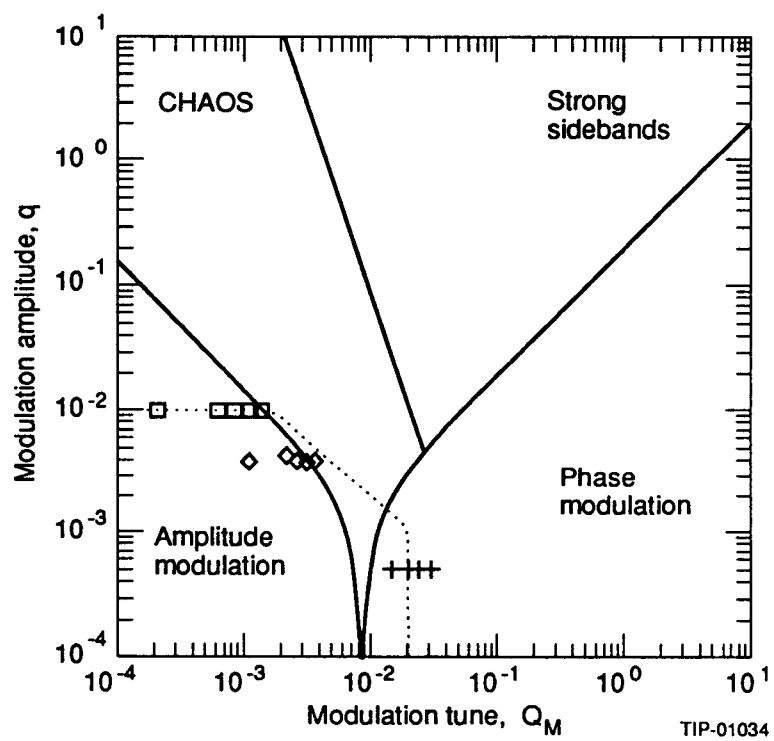

Figure 14(b). Tune Modulation Condition of the Data Shots Shown in (a).

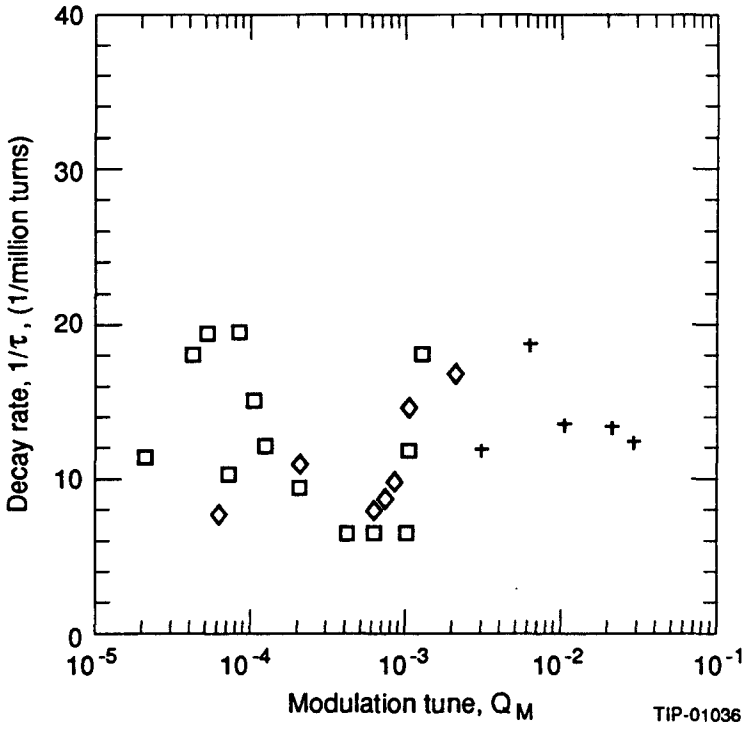

Figure 15(a). Persistent Signal Decay Rate Changing with Qm, 6.5V Data.

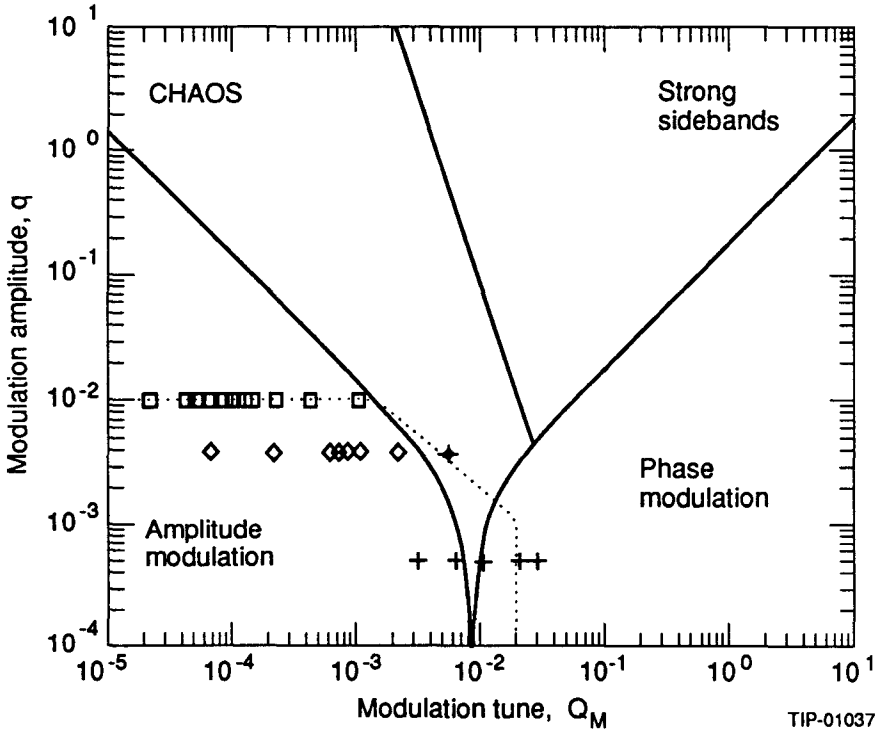

Figure 15(b). Tune Modulation Condition of the Data Shots Shown in (a).

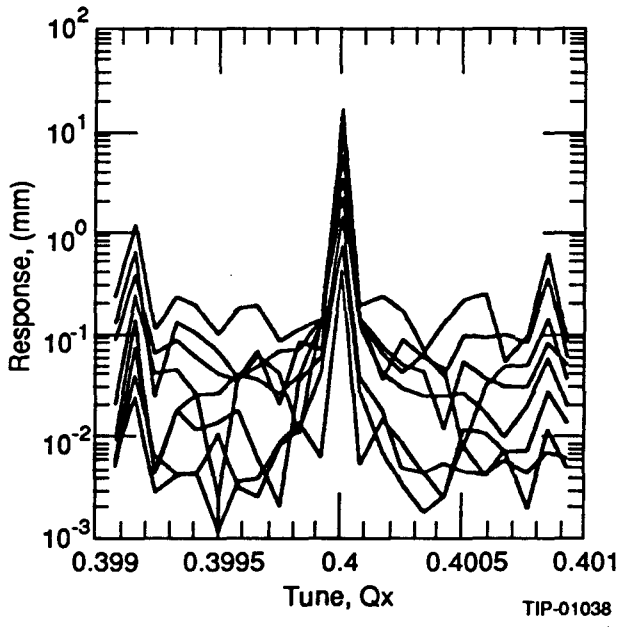

Figure 16. The Modulation Sidebands, Frequency Interval is 1/Qm.

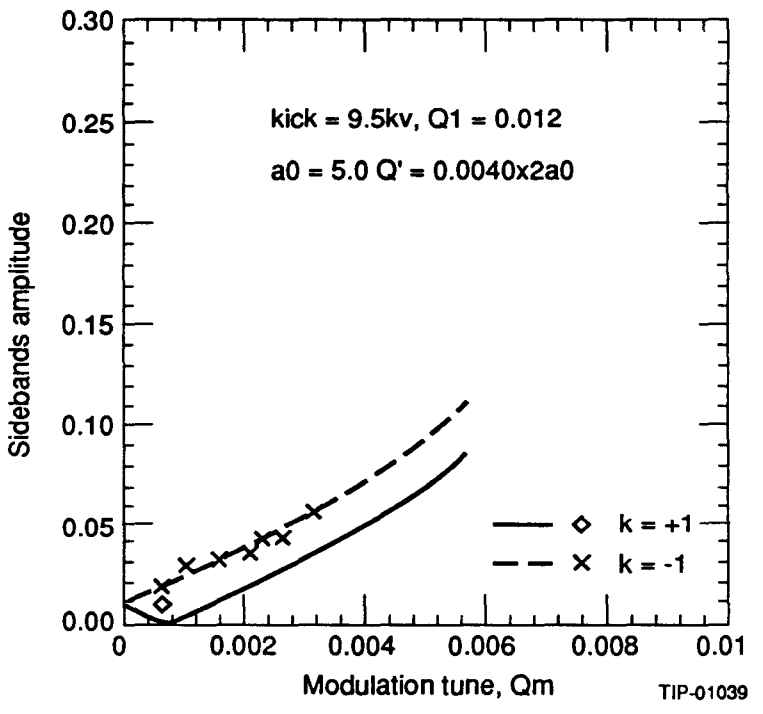

Figure 17(a). Measured Modulation Sideband Strength, with 9.5kv data. Theoretical results are fitted to the data by changing Qm.

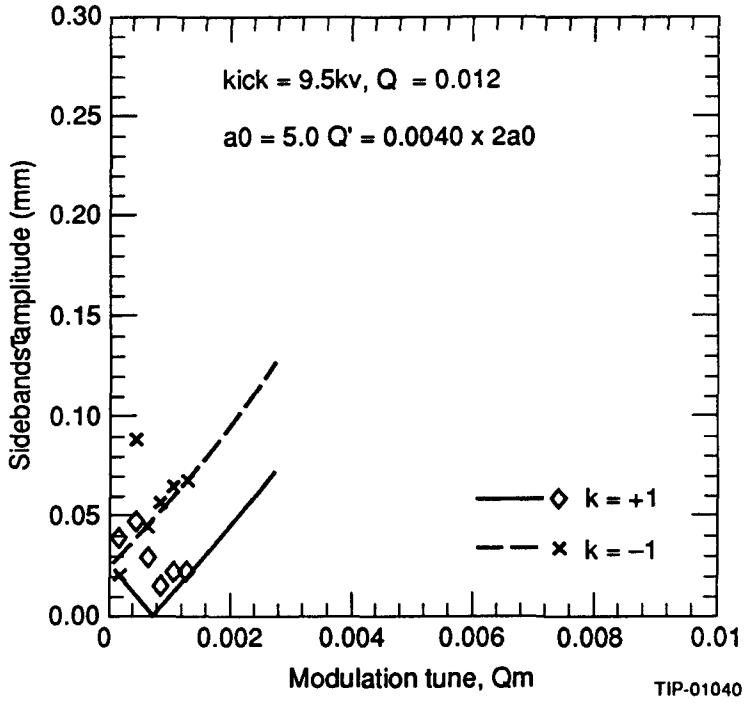

Figure 17(b). Measured Modulation Sideband Strength with 8kv data. Theoretical results are fitted to the data by changing Qm.

3.1.3 Synchro-Betatron Sidebands

Another important phenomenon expected to be found in the experiment is the "synchro-betatron sideband." In phase space, the sidebands are some stable islands if they are observed every modulation period. Particles trapped in these islands generate signals with special frequencies. These frequencies are equally spaced around the main resonance frequency, similar to sidebands. The frequency space is integer numbers of modulation frequency divided by the order of the main resonance. The frequencies can appear independently, because particles trapped in a particular island will generate one of the frequencies, unlike the modulation sidebands, which are usually generated as symmetrical pairs.

In q–Q_M space, the strong synchro-betatron sidebands appear at the top-right corner, but experimental hardware limits the experiment at the bottom-left corner. The dotted line in Figure 13(b) gives the approximate region available for the experiment. This means that the experiment so far did not provide data in a good condition to observe the sidebands. To improve the situation, either upgrade the hardware for a higher frequency and stronger modulation, or find a sextupole configuration with a lower Q_I.

At any rate, the existing data was analyzed to look for the sidebands. Two events have been found. One of them, data file number *tape15.178*, shows a clear sideband at k = +1 position. Figure 18 is its mountain-range spectrum picture; each spectrum line corresponds to one time slice, and the spectrum lines are plotted with vertical shift according to their time sequence. In the center of the picture, a series of sharp peaks presents the 2/5 resonance. The series peaks at the right side have an exact frequency space

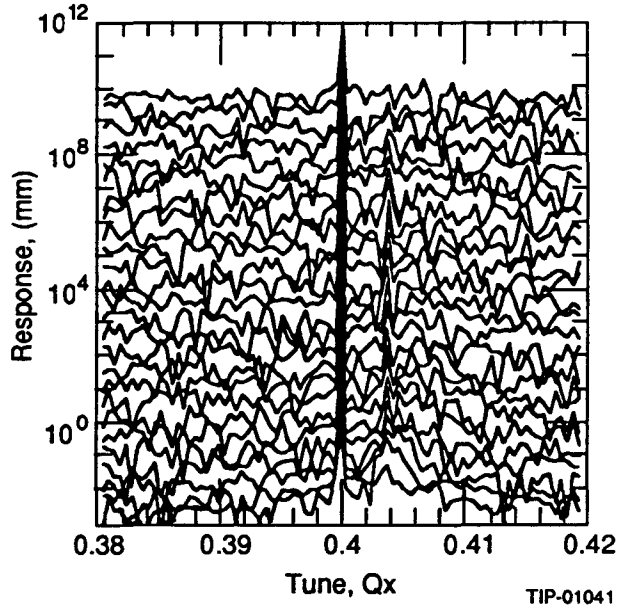

Figure 18. Spectrum Plotted as Mountain Range with Time Advance. A resonance sideband shows up with frequency space Qm/5 from 0.4.

from the 2/5 resonance as theoretically predicted. This is important evidence of the existence of synchro-betatron sideband.

The file *tape15.179* is from the same experiment shot, but taken from a different CAMAC station-CAMAC9, which is more sensitive and clearer. Figure 19(a) shows the result of this data file. The sideband looks clearer. At the very left and right side of the spectrum, the modulation peaks can be seen. Their frequency spaces from 2/5 resonance are tune modulation frequency, 5 times larger than the synchro-betatron sideband. Figure 19(b) is the time variation of the spectrum amplitude at every frequency where the sidebands are supposed to be found. The line at the top is the 2/5 persistent signal. Its slope indicates the decay rate of the persistent signal. The line in the middle is the amplitude of the sideband. It is obviously much higher than the others (note that the vertical coordinate uses log scale). Figure 19(c) shows the sideband phase versus time. If the signal has a certain frequency, it should be phase-locked; that is, its phase shouldn't vary with time. The straight line in the picture is the phase of 2/5 signal, and it is well locked. The other line is the phase of the sideband at the right side of the 2/5 peaks. It is also locked, so that the sideband is proven to be a real signal.

The experimental conditions of this data set are: tune modulation frequency (in tune unit) $Q_M = 0.0189$, modulation amplitude $q = 0.00052$, horizontal emittance generated by collimator is 6π, the basic tune settled to the machine is $Q_x = 19.439$ and, kick voltage is 8 kV. The position in Figure 14(b) is the second + from left. It is in the phase modulation region, where the sidebands are weak because they are suppressed by the Bessel function. It is difficult to say how strong a sideband can be observed in the experiment.

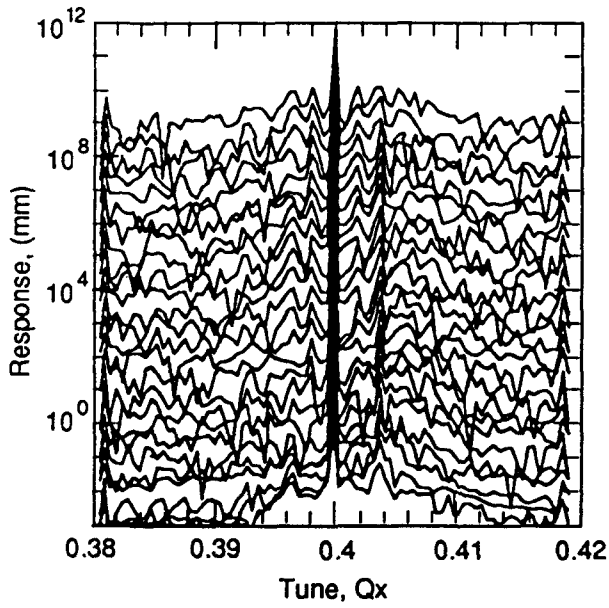

(a) Mountain range spectrum.

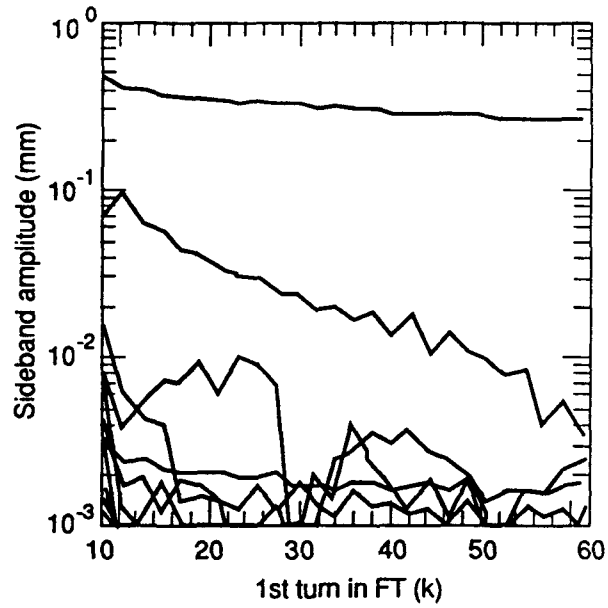

(b) Sideband strength versus turn number.

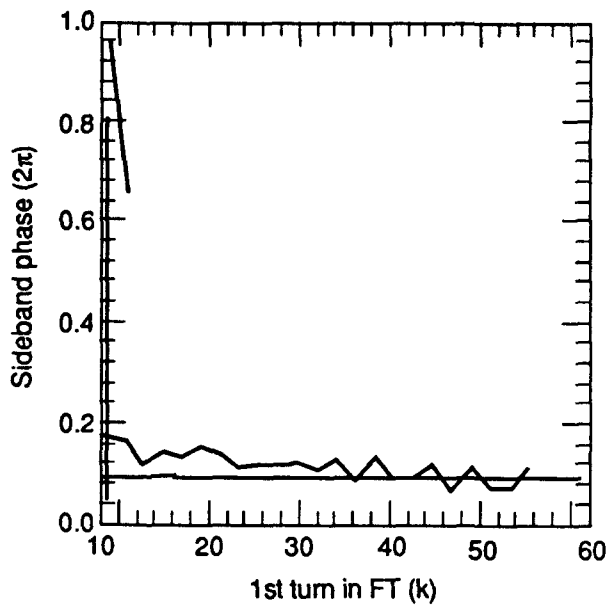

TIP-01042

(c) Sideband phase versus turn number.

Figure 19. Mountain Range Spectrum (data taken through CAMAC 9).

The other event where the sideband appears is *tape16.169*. The interesting thing is that in this shot, there is no 2/5 persistent signal, but a clear signal appears at the frequency which has a 3/5 Q_M shift from 2/5. Figure 20 shows the results. Similar to the first event, another file, *tape16.170*, same shot but taken by CAMAC 9, shows a clearer signal (Figure 21). In this picture, one more series of peaks appears at 2/5 – 2/5 Q_M.

Because it has a frequency space of Q_M from the sideband, it can be explained as the modulation sideband of the synchro-betatron sideband shown in this data set.

This particular case can be explained in the following way. The beam was kicked into the particular sideband island, but not in the 2/5 resonance island. Under this condition, this sideband island is stable, but others are unstable. According to the condition, $Q_M = 0.00525$, $q = 0.004$, this shot is in the chaos region. Its position in q–Q_M space is shown in Figure 15(b) as a star. In this region, the motion is chaotic because of overlapping sidebands. It is possible that the kernel of some sidebands do not overlap completely, as shown in Figure 9(d).

3.2 Results of the Experiment in June 1989

In the 1989 run of E778, we planned to do the experiment of 2-D resonance, diffusion, mockup SSC, and resonance island (tune modulation). In the resonance island experiment, the sextupole configuration is different from the one used in the 1988 E778 run. The difference: all the power supply polarities of the opposition section are inversed, i. e., the polarities in F section are (+–+–+–+–), but in C section are (–+–+–+–+). This so-called 891 configuration provides much larger 2/5 resonance islands than the 88 configuration. During the run, because of machine condition and equipment problems, some experiments were shortened or cut, and some data were lost. Following is the data analysis of the island experiment.

3.2.1 Data Structure and Calibration

During this E778 run, data was recorded by 8 channels. H_44A, H_44B, V_45A, and V_45B are taken through CAMAC station 5, and H_42A, H_42B, V_43A, and V_43B are taken through CAMAC station 9. The length of each object can be 16K, 32K, or 64K. The two horizontal beam position signals are calculated by:

$$X_1 = \frac{H_42A - H_42B}{H_42A + H_42B} \times CC9$$

$$X_2 = \frac{H_44A - H_44B}{H_44A + H_44B} \times CC5,$$

where CC5 and CC9 are calibration factors.

To calibrate the equipment, a few dipoles are used to generate a ±10 mm bump at BPM's position. Data shots were recorded during the bump ramping. Figure 22 shows the recorded bump. The top and bottom of the ramp should correspond to ±10 mm beam position deviation, respectively. Table 1 gives the results of the calibration data.

Because the calibration factors are so different under different conditions, the result is not good enough to apply them in data analysis.

Table 1. Results of Calibration Data.

shot #	Intensity (10^{10} p)	CC9	CC5
16	0.7	888.9	108.5
17	0.8	294.1	52.2
18	---	348.4	48.3
19	0.5	95.8	72.2
20	1.4	1626.0	40.5

In practice, the calibration factors are chosen as CC5 = 266.7, CC9 = 333.3. The reason for choosing these numbers is that they put the value of x_1 and x_2 in a reasonable range, and make the phase space look reasonable. In fact, the data analysis is mainly concentrated in Fourier transform of x; the absolute value is not important in this sense.

The chirping experiment has a different data acquisition arrangement. There are two channels in CAMAC 5, recording H_44A, H_44B, 256 K turns each. The second channel of CAMAC 9 recorded the chirping signal, i.e., the a.c. current applied to the tune modulation quadrupole. Because there is only one BPM signal recorded, it is impossible to work out the phase space. However, we just need the Fourier transform of one beam position signal, and its absolute value is not important.

3.2.2 Frequency Scan Experiment

In this experiment, a dipole kicker driven by an alternative current "shakes" the beam. The driven frequency scans around the fractional tune. Its effects on resonances are going to be observed. Some other resonances—for example, 5/13 resonances—are expected to be excited.

In this experiment, the persistent signal dropping down a little when the exciting frequency scans across $\nu = 0.4$ has been observed. After the frequency passes the resonance point, the persistent signal maintains its amplitude. Figures 23(a) and 23(b) show the persistent signal amplitude versus turn number of two data shots. In Figure 23(a), the frequency scans from 18.0–18.8 kHz, or 0.383–0.4 in tune unit. In Figure 23(b), the frequency scan range is 18.4–19.2 kHz, 0.391–0.409 in tune unit. In both shots it is observed that persistent signal amplitude drops and stays constant. Because the start values of frequency scan are different, the dropping time (or turn number) is different.

The 5/13 resonance can be observed in most data shots. Figure 24 shows the mountain range spectrum of beam position signal. A series of peaks at 0.3846 is obvious. Although the 5/13 resonance signal is much weaker than 2/5 resonance, the figure also shows that its amplitude is much higher than noise, and its phase is locked.

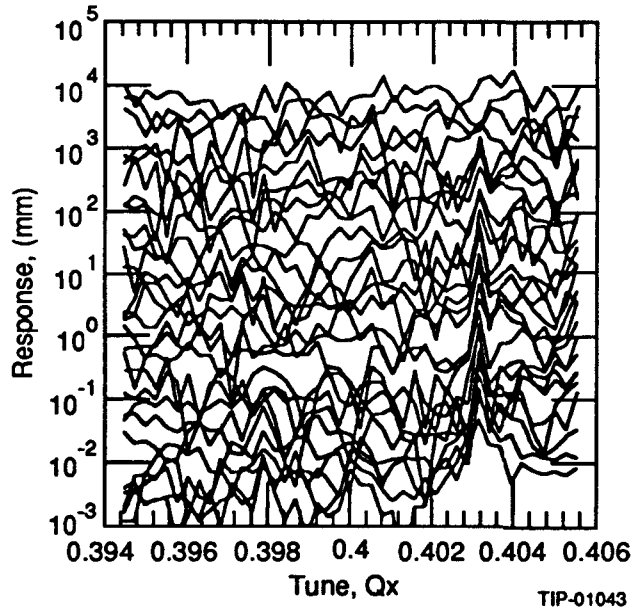

Figure 20. Mountain Range Spectrum Without 2/5 Resonance Peaks, but with a Sideband at $0.4 + \frac{3}{5}$ Qm.

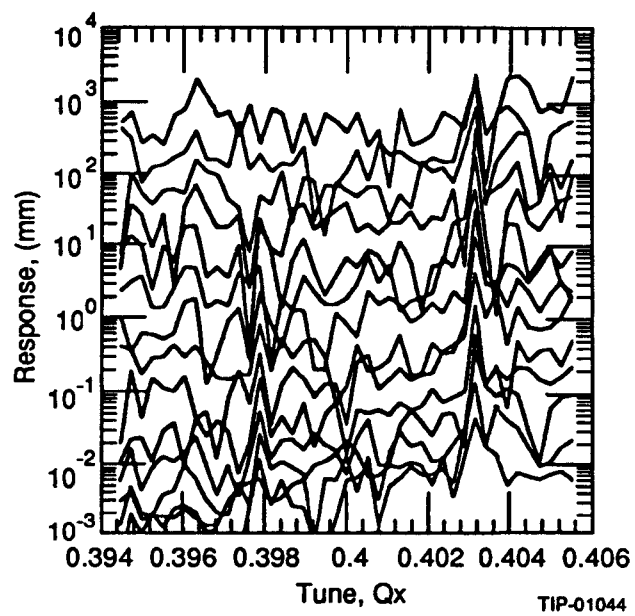

Figure 21. Mountain Range Spectrum Without 2/5 Resonance Peaks, but with a Sideband at $0.4 + \frac{3}{5}$ Qm (data taken through CAMAC 9).

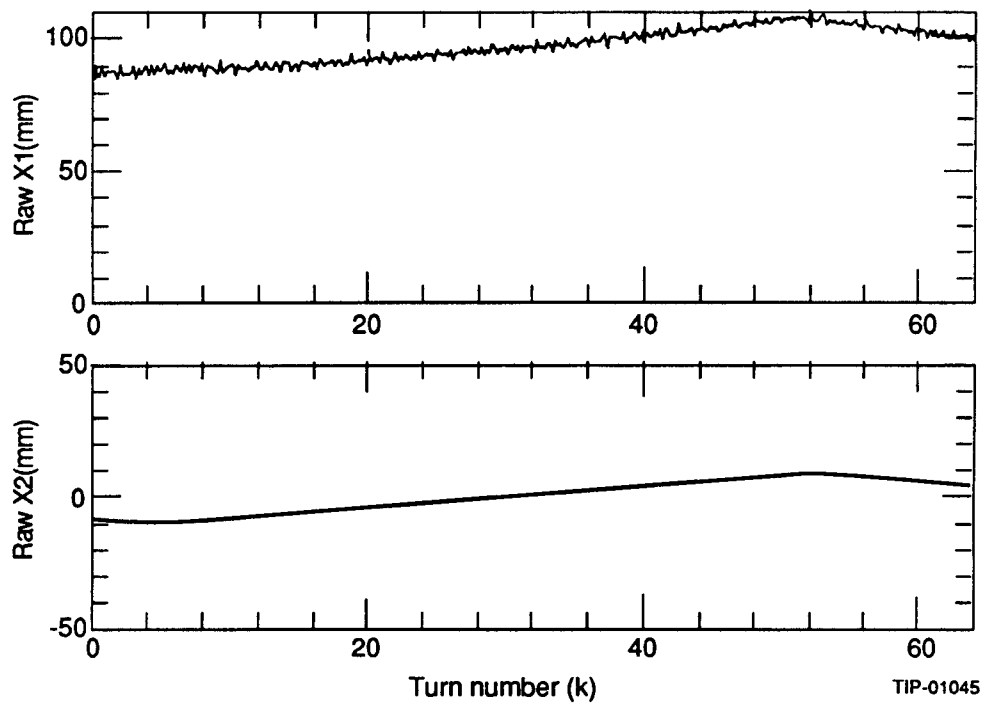

Figure 22. Calibration Bump Recorded by Data Acquisition System.
Upper: F42H through CAMAC 9
Lower: F44H through CAMAC 5

By observing the amplitude spectrum, many shots show a peak at $\nu = 0.00635$. It may be a sign of Q_I, because the island size of this sextupole configuration is much larger, and the pencil beam can circulate inside the island. But it is not strong enough to be evidence; only the peak's consistency in frequency rises concern.

3.2.3 Chirping Experiment

The purpose of this experiment is to measure Q_I, and to prove tune modulation theory. The idea is that if changing tune modulation frequency and amplitude are ramped right after the kick, as soon as the modulation conditions reach the chaotic boundary, the persistent signal should drop down very fast. Q_I should be found by matching the boundary to modulation conditions when the persistent signal drops down.

The tune modulation conditions, q and Q_M, are achieved by Fourier analysis of driving signal. Consider that the frequency change can be ignored during the period for doing FFT, and Q_M can be calculated directly, but modulation amplitude q needs calibration. As we know, 25-ampere current applied to this particular quadrupole gives a tune variation of 0.0083. In the experiment, the current was ramped from 0 to 25 amp, but in fact the current is not ramped linearly because of frequency response. There are two frequency ramping ranges used in the experiment, 0–30 Hz and 0–300 Hz. The 300 Hz ramp shows a serious amplitude suppress for high frequency, but 30 Hz looks good. Suppose the 30 Hz ramp reaches 25 amp at the end, making the recorded data amplitude, 10.29,

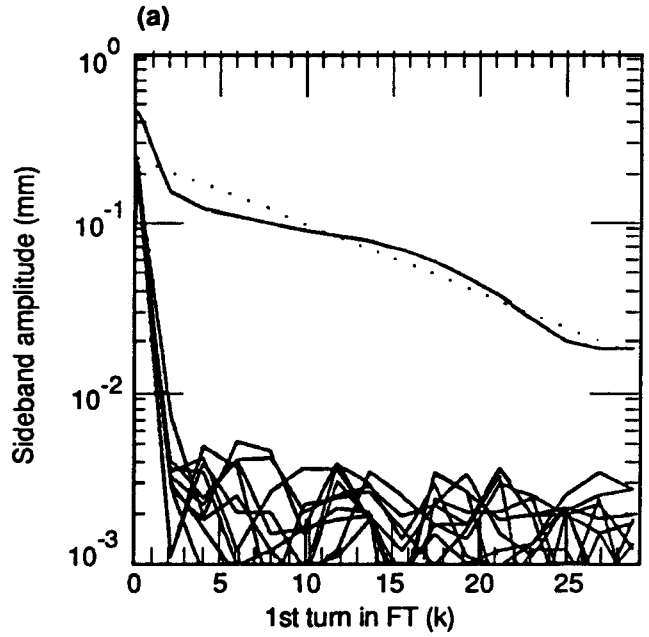

Figure 23(a). Persistent Signal Amplitude Versus Time with Frequency Scanning (frequency scan 18.0-18.8 kHz).

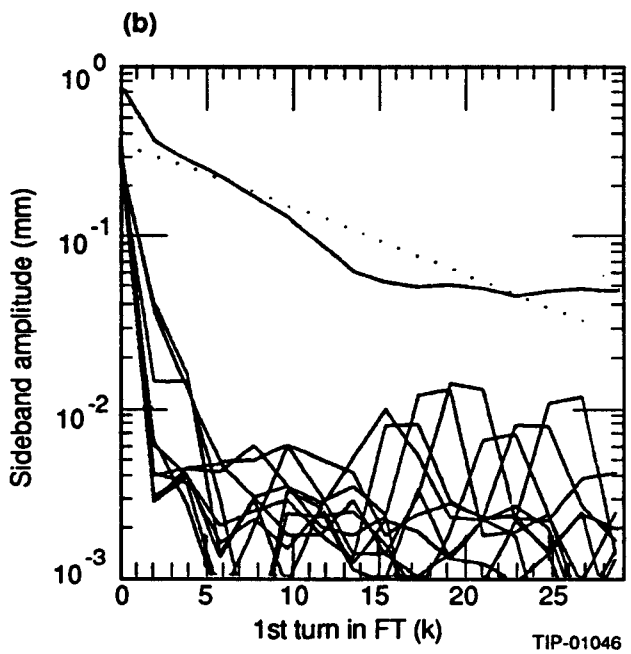

Figure 23(b). Persistent Signal Amplitude Versus Time with Frequency Scanning (frequency scan 18.4-19.2 kHz).

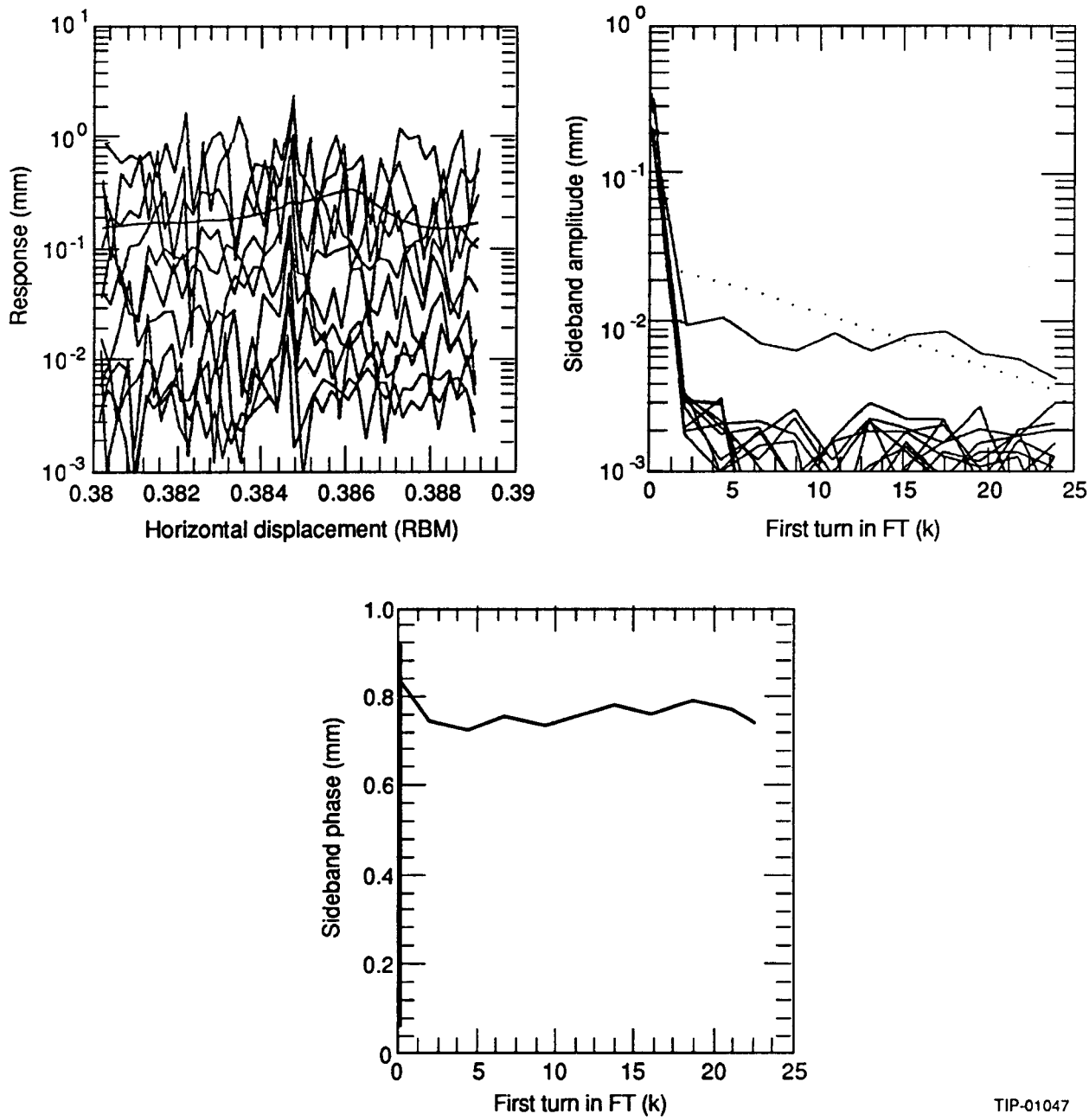

Figure 24. The 5/13 Resonance.

which is calculated by FFT, equivalent to 25 amp current. So, 10.29 FFT amplitude is equal to 0.0032 tune modulation depth.

The experimental data performs very well. Figure 24 is a typical result from one of the data shots. In the mountain range picture, the peaks at 0.4 disappeared in the middle. In the amplitude versus turn number (or time) picture, the amplitude dropped down rapidly. At the mean time, its phase was unlocked. These phenomena demonstrate that the persistent signal is gone. The resonant island is not stable anymore. In other words, the modulation conditions hit the chaotic boundary.

Table 2 lists the modulation conditions when the persistent signal is gone.

Table 2. Modulation Conditions.

Shot No.	Qxo	q	Qm	Qi
shot0	0.428	0.00354	0.00195	0.00619
shot2	0.428	0.000526	0.00464	0.00581
shot3	0.428	0.00204	0.00244	0.00555
shot4	0.428	0.00681	0.000488	0.00411
shot5	0.428	0.00146	0.00439	0.00716
shot8	0.426	0.000533	0.00464	0.00582
shot9	0.426	0.00260	0.00220	0.00578
shot10	0.426	0.00683	0.000488	0.00411

Shot-1 has the persistent signal during the time the data was taken. The reason is the modulation conditions do not reach the chaotic boundary.

Shot-5 had a very fast ramping of 0.1 second. Even in this short period, it is observed that the persistent signal dropped in 4500 turns. This shot may have a big error bar because of fast changing of frequency, but it provides more evidence for the chirping experiment. Figure 25 is the plots of shot 2.

Put the data results in q_Q_M plot, and give a proper Q_I by which the boundaries are plotted to fit the data points. Figure 26 is the plot. The Q_I selected here is 0.006. Q_I can also be calculated by using the boundary condition

$$Q_I = \sqrt{Q_M^2 + 5qQ_M}. \qquad [53]$$

The results are also listed in Table 2. Average Q_I is 0.00557, with an error of ± 0.001. This is the first time we obtained a proper value of Q_I by measuring it in experiment.

There are still some problems about the results. The measured Q_I, 0.006, is about half of EVOL simulation result. The reason is under study. The other problem is that as the basic tune Qxo was changed by 0.002, there should be a change in Q_I. EVOL tracking results show that if basic tune changes from 19.41 to 19.412, Q_I will change from 0.0115 to 0.0148. This is an obvious change, but it doesn't show in the experiment result.

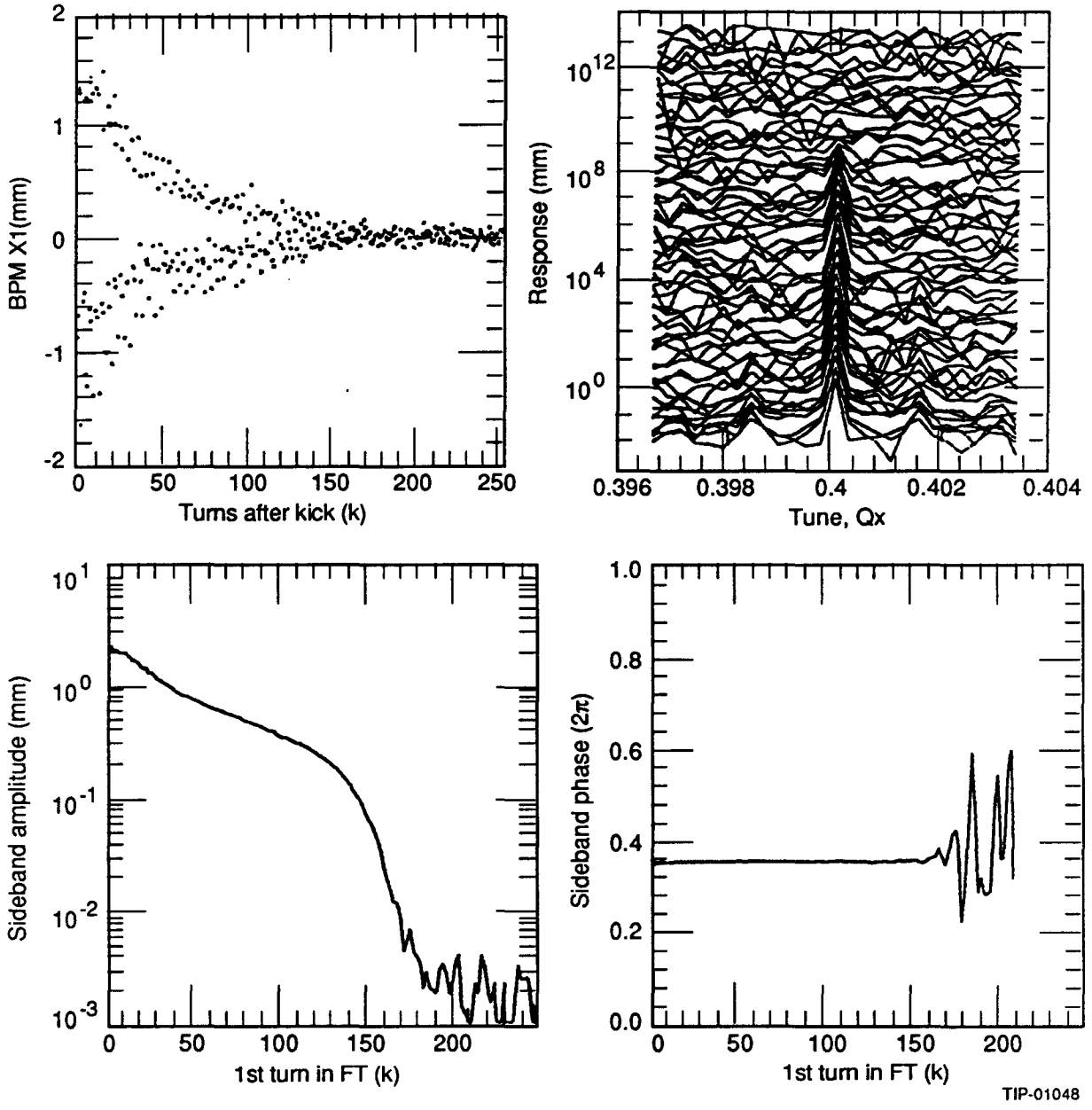

Figure 25. Persistent Signal Drop.

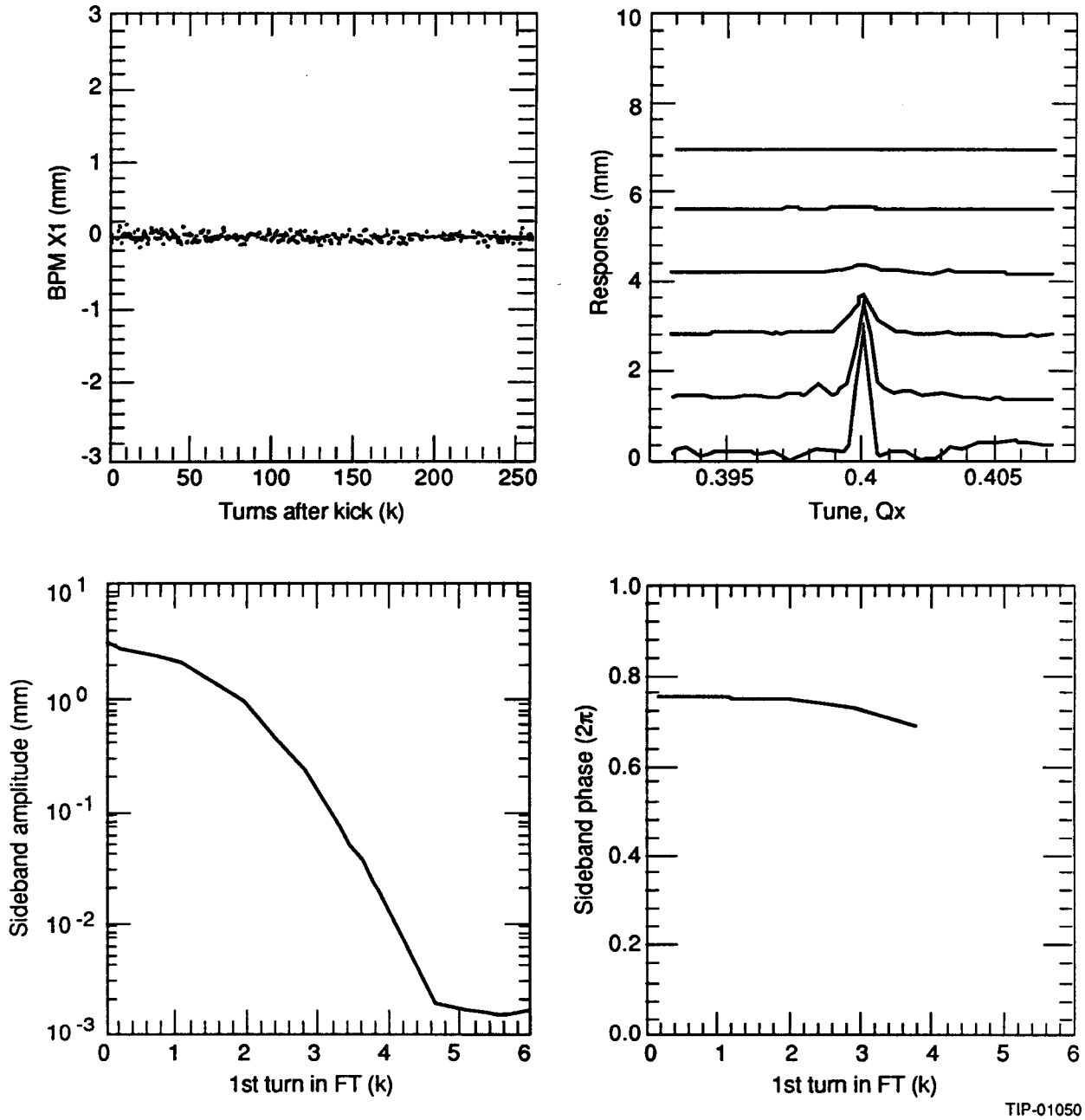

Figure 26. A Data Shot with Fast Persistent Signal Drop.

4.0 SEXTUPOLE CONFIGURATIONS IN E778

The nonlinear resonances, especially higher-order resonances, are strongly dependent on the phase relation and polarities among sextupoles, because sextupoles drive 3rd order resonance directly; but their cross terms drive 4th and 5th order resonances. It is very hard to find a simple parameter which describes the driven strength to any particular resonance. And it is hard to calculate the higher order resonances by perturbation method. In this case, tracking is more effective. As the phase advances between sextupoles are fixed, the polarity configurations significantly effect detuning, island size, Q_I, etc. The polarity configurations of sextupoles are investigated for the June 1989 run of E778.

The 16 sextupoles are set in F and C sectors of the Tevatron. They are powered in pairs by 8 power supplies. Table 3 lists some possible configurations investigated.

Table 3. Possible Configurations of Sextupoles.

Config. no.	F	C
88	+ − + − + − + −	+ − + − + − + −
890	+ + + + + + + +	− − − − − − − −
891	+ − + − + − + −	− + − + − + − +
892	+ − − + + − − +	− + + − − + + −
893	+ + − − + + − −	− − + + − − + +
894	+ − − + + − − +	+ − − + + − − +
895	+ + + + + + + +	+ + + + + + + +
896	+ + − − + + − −	+ + − − + + − −
897	+ + − − − − + +	− − + + + + − −
898	+ + − − + − + −	− + + − + + − −

The two important resonances in E778 are 1/3 and 2/5. The phase advance between two adjacent sextupoles is 68°. For 3rd order resonance, 3ψ=204°, which is not too far from 180°. As a result, if two adjacent sextupoles have the same polarities, the two vectors will almost cancel each other. But if they have opposite polarities, the two vectors will add up, so that a strong 1/3 resonance will be driven.

The phase advance between F and C sector is $9.7 \times 360°$. To consider the 5th order resonance, the fractional part of 5ψ is just about 180°. To drive the 2/5 resonance, the two sextupoles that have the same station number, but in F and C sectors, respectively, should have opposite polarities.

The chromaticity caused by the special sextupoles is proportional to the dispersion function at the sextupole locations. The dispersion function is almost the same in the F sector as in the C sector, but it is not regularly distributed within the sectors. Therefore, to minimize the chromaticity produced, the polarities of the sextupoles with the same station number, but in F and C sectors, respectively, should be opposite.

The features just described for the sextupole configurations considered are shown in Table 4. The resonance excitation is seen in the phase-space tracking results shown in Figure 27, for the Tevatron tuned to 19.41, 19.46.

Table 4. Features of Sextupole Configurations.

Config. no.	Drive 1/3	Drive 2/5	Chromaticity
88	Strong	Weak	–5.56/1.57
890	Weak	?	–0.65/0.26
891	Strong	Strong	0.20/–0.04
892	*	*	0.86/–0.53
893	Weak	Strong	–0.33/–0.04
894	*	*	27.65/–9.2
895	Weak	Weak	140.1/–46.4
896	*	*	–18.4/5.88
897	Weak	Strong	–2.15/0.49
898	**	**	–13.7/3.70

* Q_x increases with amplitude.
** Symmetry lacking.

Following are some suggestions for this E778 run.

1. Island experiment

The configuration 891 drives the 2/5 resonance and provides large islands. It is good for island experiments to measure the capture fraction, island position and width, etc. Since the island is much larger than in the configuration used in the 1988 run, the particle motion inside the island could be observable, and Q_I or decoherence in islands might be measurable. From tracking, $Q_I = 0.0115$.

The configuration 897 also drives the 2/5 resonance. Although the island size is not as large as in 891, the islands are distributed almost on a circle and are evenly spaced. This is good for comparing measurement results with computing results: resonance amplitude, and island size, for example.

Some configurations drive other resonances. For example, 890 provides large 1/3 resonance islands, and 894 gives 7th order resonance islands. They could be used for other resonance investigations.

2. Mocking up SSC

The tune shift versus smear curve is chosen as the criterion for mocking up the SSC. From tracking, we know that the SSC has relatively small tune-shift and large smear. The large smear is attributable to coupling resonances. Figure 28 shows that the 892 tune shift versus smear curve approaches that for the SSC when the basic tunes are moved closer together. Thus, adjusting the horizontal-vertical coupling can provide a tune-shift vs. smear curve similar to that of the SSC.

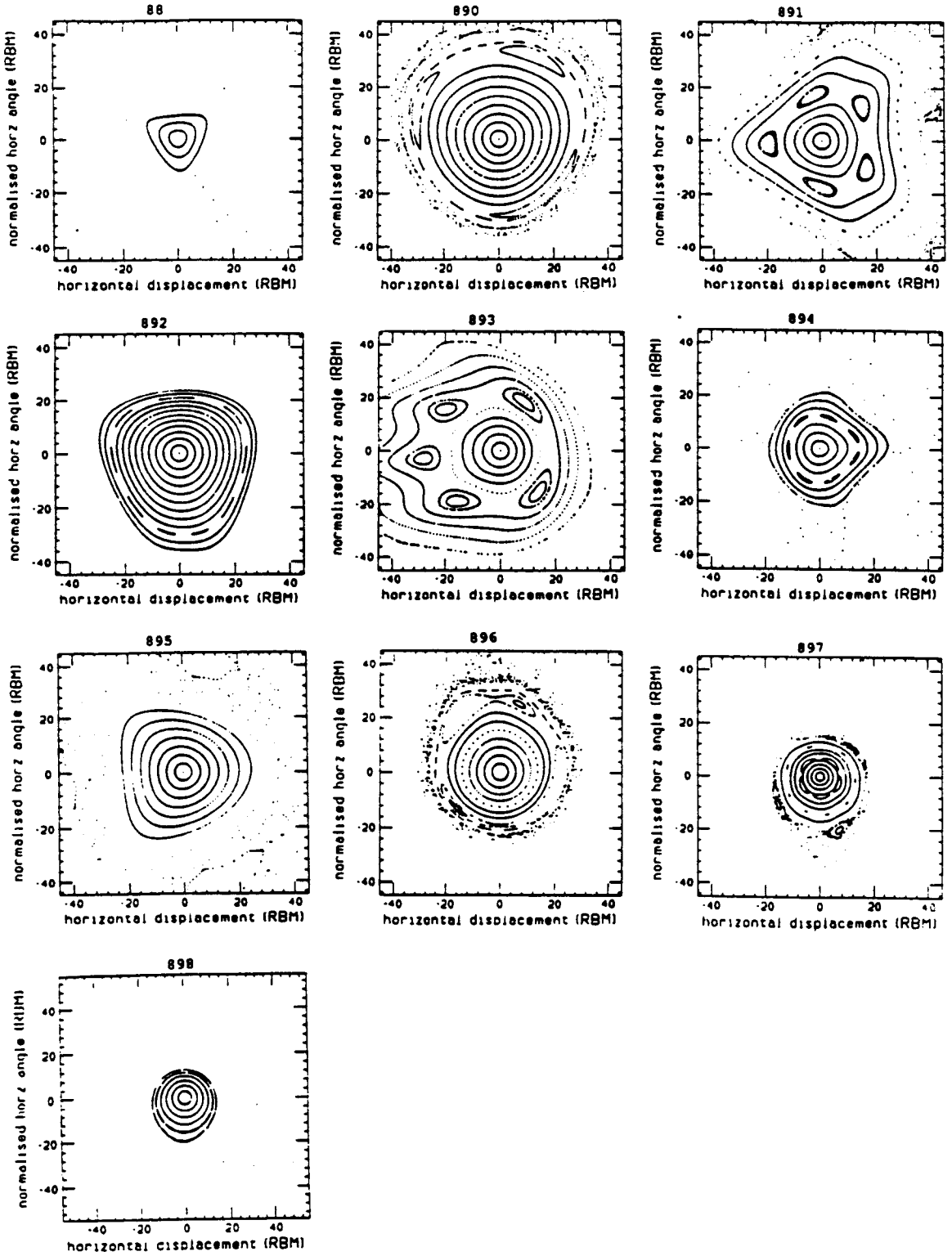

Figure 27. Phase Space Plots for Different Configurations.

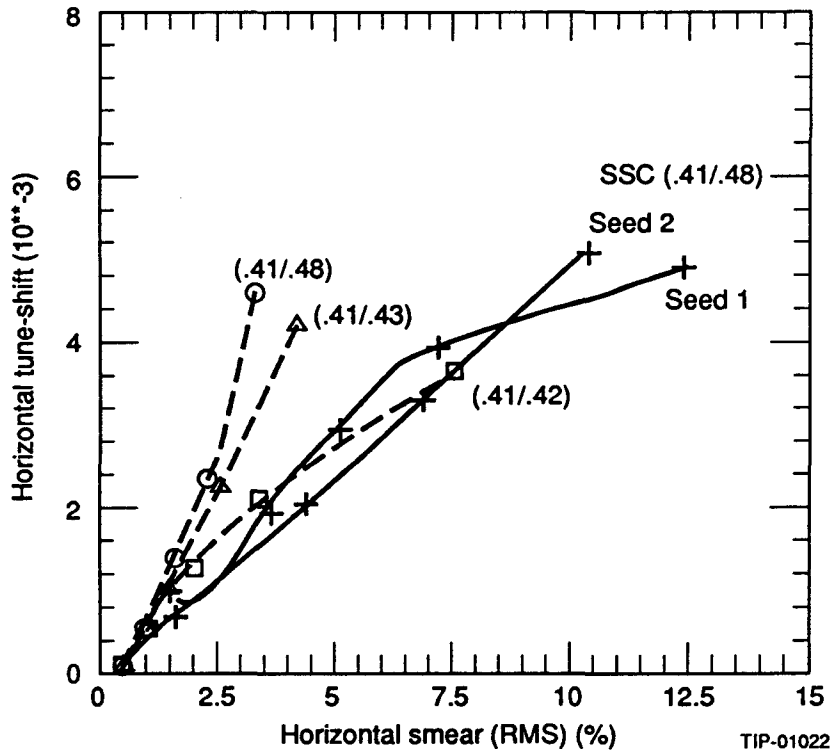

Figure 28. Tune Shift vs. Smear of SSC and 892.

Most of the configurations have higher tune shift versus smear curve than the SSC. To get a lower curve, a fancy configuration--898 was found. Figure 29 shows the results.

3. Two-dimensional resonances

To study what can be observed about 2-D coupling resonances, some 2-D tracking calculations were performed, and betatron phase ψ_y vs. ψ_x plots were displayed.

Figure 30 illustrates the case in which there is resonance in the x plane only. Islands are observed in the x-plane, but not in the y-plane.

Figure 31 shows similar plots for the $Q_x - Q_y$, and $2Q_x - Q_y$ resonances. The bands show that the two phases are correlated. No islands can be observed.

Figure 32 is a special case: $q_x = 0.2$, $q_y = 0.4$, so that the particle is involved in three resonances: $5q_x = 1$, $5q_y = 2$, and $2q_x - q_y = 0$. In ψ_y vs. ψ_x space, there are intermittent bands. And islands can be observed in both planes.

Generally, it is advantageous to observe ψ_y vs. ψ_x space to find the coupling resonances.

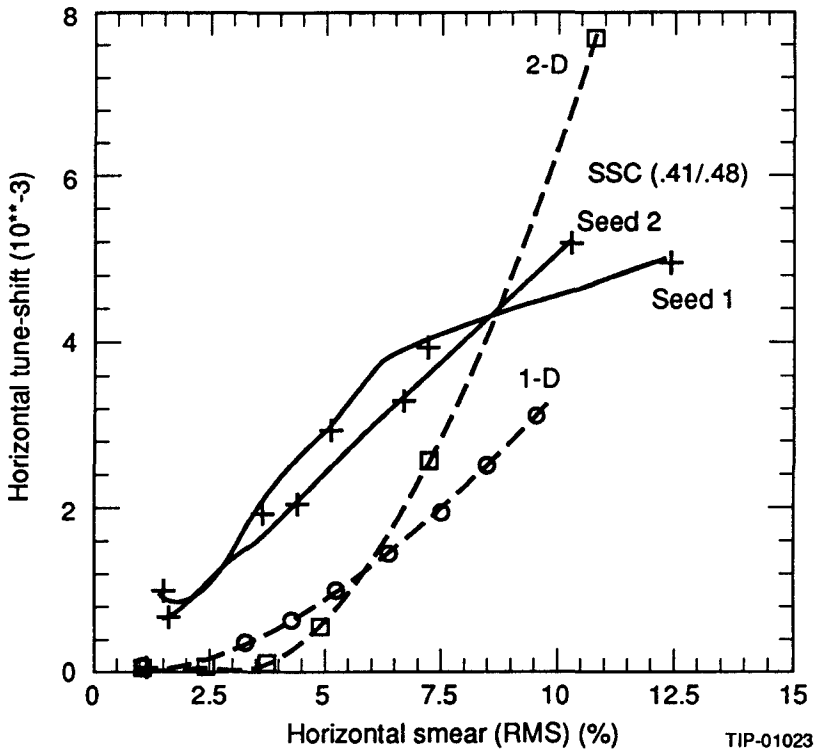

Figure 29. Tune Shift vs. Smear of SSC and 898.

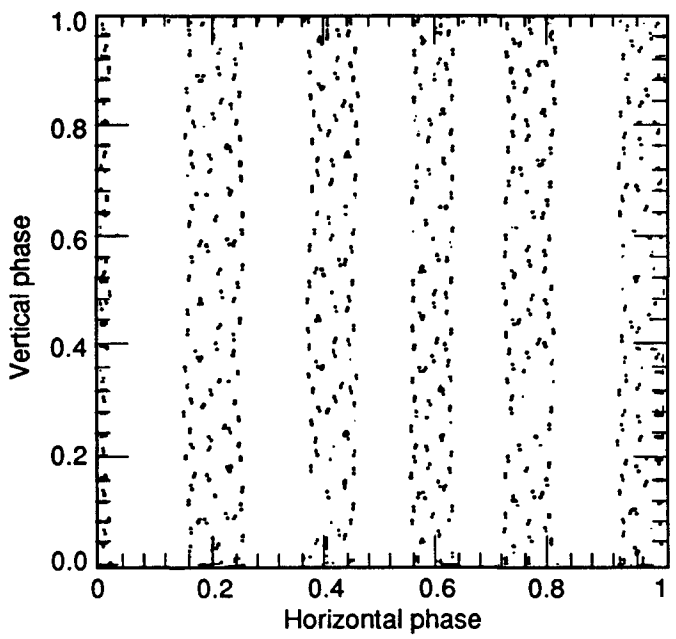

Figure 30. Betatron Phase Plot with 1-D Resonance Only.

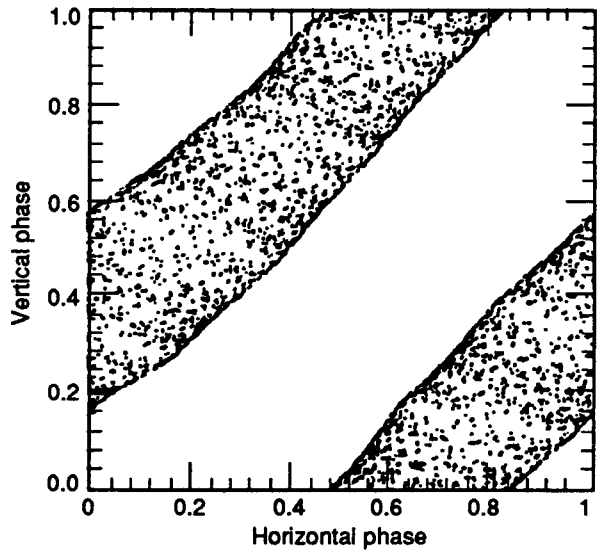

(a)

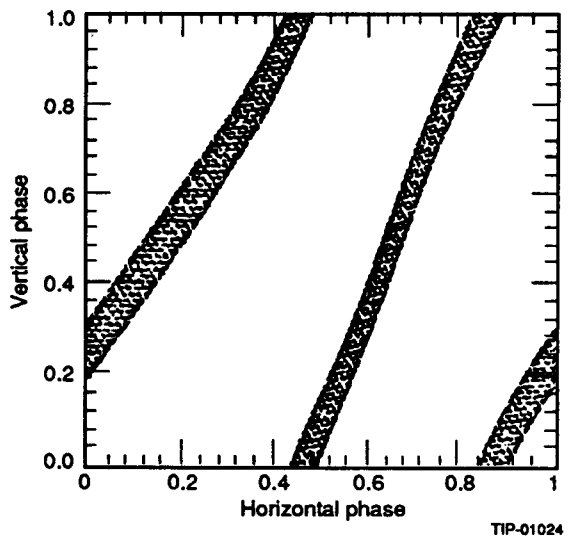

(b)

Figure 31. Betatron Phase Plot with 2-D Coupling Resonances.

(a) for $Q_X - Q_Y$, (b) for $2Q_X - Q_Y$.

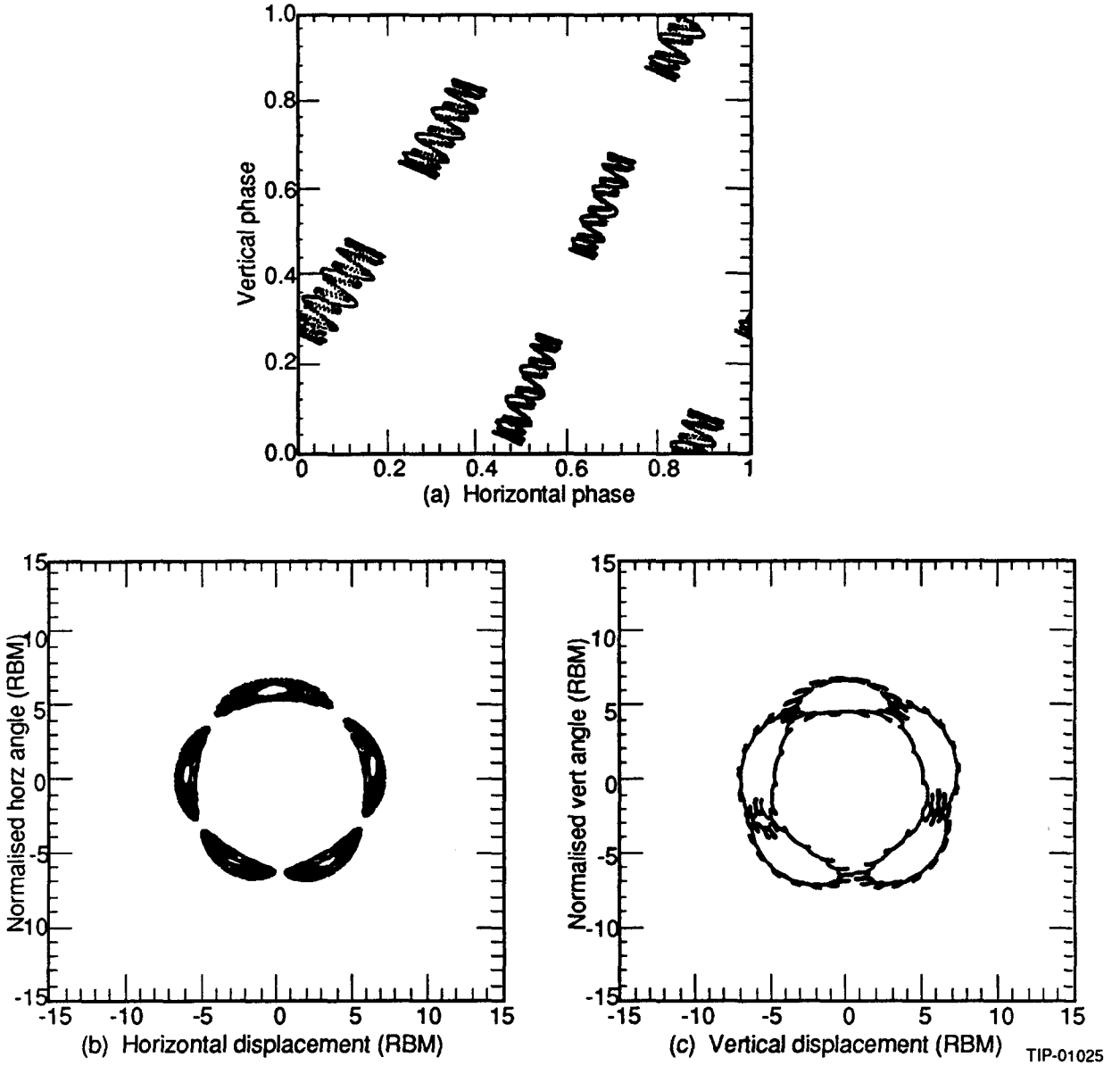

Figure 32. Betatron Phase Plot with Three Resonances:
(a) $5Q_X = 1$, (b) $5Q_Y = 2$,
(c) $2Q_X - Q_Y = 0$.

5.0 DYNAMIC APERTURE

The study of magnet aperture is the most important topic in the SSC conceptual design. To determine the linear aperture, E778 has included some experiments for smear, tune shift, and decoherence time. The results have shown good agreement between measured and computed values. However, the experiment on dynamic aperture shows only qualitative agreement between measured and computed values. For example, the tracking result shows that the dynamic aperture is 12.5 mm at HC48 flying wire under 25 amp sextupole strength, but the measured value is 10 mm. More long-term behavior has to be investigated. So far, this is limited by computer capacity.

EVOL, even though it is not an element-by-element tracking program, is an acceptable model, and a very efficient code. By using EVOL, it is possible to compute over times which normal tracking programs cannot reach. To determine the long-term dynamic aperture of E778 experiment, up to 5×10^6 turns were tracked. That means more than 100 seconds of Tevatron running time. Comparatively, that means about 25 minutes of SSC running time. Another advantage to using EVOL is that it is easy to include tune modulation effect (or so called ripple effect). This is important in long-term beam dynamic study.

EVOL was modified to do the long-term tracking. The memory space was enlarged, and an output file, *lost.out,* which records the amplitude and turn number when a particle gets lost, was provided. Particles are launched from large amplitude to small amplitude, one by one. The program will stop when 10 consecutive stable particles are found. The dynamic aperture versus turn number can be plotted by using the data in *lost.out* file.

In order to compare the computing value and experimental measured value, it is necessary to find out the relation between launched amplitude and full width at flying wire HC48. This relation is not simple because of the substantial non-linearity of the phase space. This relation is found by tracking. Figure 33 shows the result.

Figure 34 is the dynamic aperture versus turn number with different amplitude of tune modulation. The solid line indicates the case without tune modulation. The dynamic aperture at the HC48 flying wire is 12.5 mm in full width, which agrees with TEAPOT tracking result. There is almost a vertical line at the dynamic aperture when the turn number increases. It therefore appears that long-term behavior will not shrink the dynamic aperture much. More investigation is needed. For example, does the more precise element-by-element tracking show the same result? Does this result depend on sextupole configurations, which resonance the tune is close to, coupling between two planes, or tune shift, smear, etc.

The dashed line and dotted line describe tune modulation. The larger the modulation amplitude, the smaller the dynamic aperture. Notice that many particles get lost within the first period of tune modulation. Although the dynamic apertures are smaller, they do not quite depend on turn number. In other words, dynamic aperture does not shrink significantly as turn number increases. If this is proven, it would give more confidence to the SSC design.

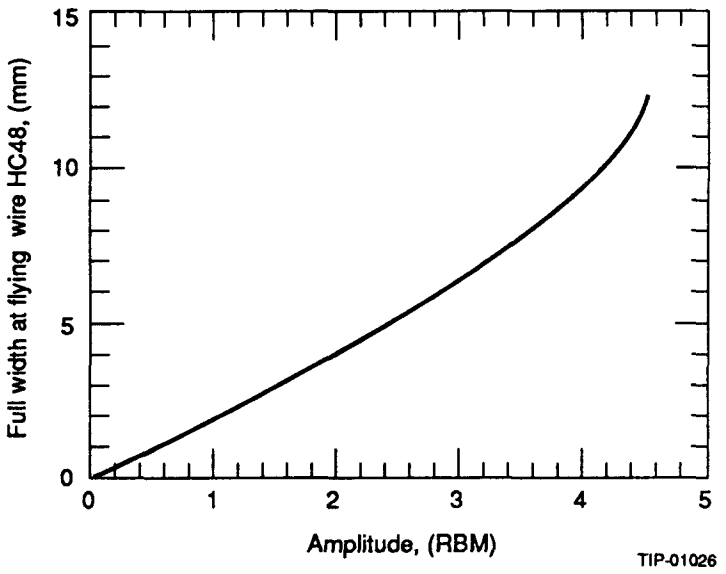

Figure 33. Relation Between Launched Amplitude and Full Width at Flying Wire HC48.

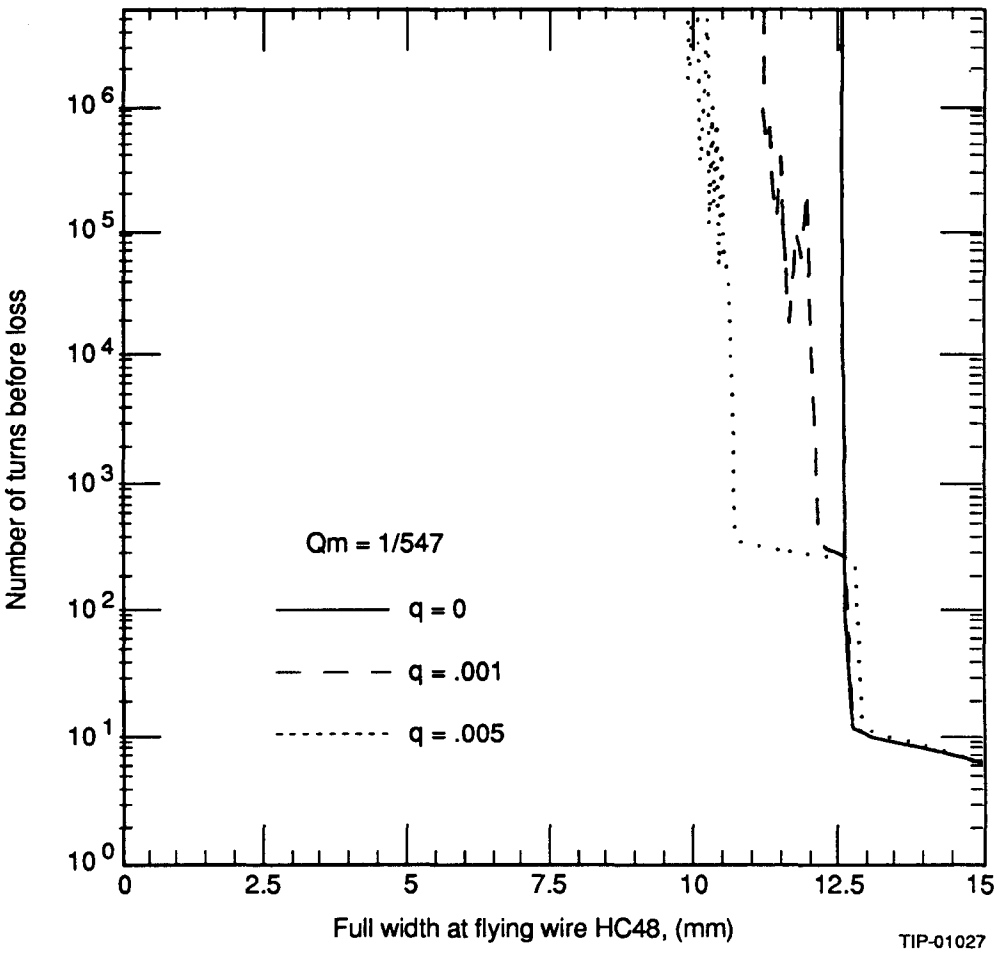

Figure 34. Dynamic Aperture with Different Amplitude of Tune Module.

The study of two-degrees of freedom has also been investigated. By "two-degrees" here, we mean that initial amplitudes in both x and y plane are non-zero. Note that there is no coupling field in EVOL. Figure 35 compares the dynamic apertures of the particle launched in x plane only and in both x and y plane. The figure shows that the dynamic aperture is reduced by 2-D motion, but the long term behavior remains good. Figure 36 gives the results of two-degree motion with tune modulation. The dashed line is the case of two-degree motion with tune modulation in one plane. The dotted line is the case where tune modulation is introduced in both planes. The one-degree result is plotted by a solid line as a reference. The dynamic aperture is reduced again by two-degree motion and tune modulation, and it decreases as the turn number increases in the range of 10^4 to 10^5 turns, which is the range a normal tracking program can reach. But dynamic aperture does not change much beyond 10^5 turns.

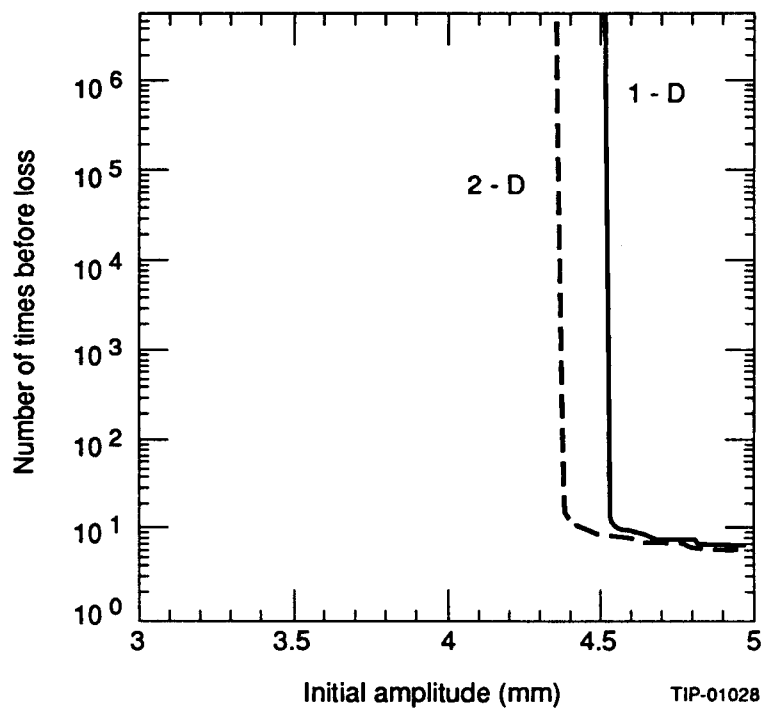

Figure 35. Dynamic Aperture for One-Dimension Motion and Two-Dimension Motion Without Tune Modulation.

A similar experiment was done on SPS. Studies for that experiment also show the important effect of tune modulation (or ripple) and coupling. Figures 37 and 38 show a tracking result for SPS experiment. One is from EVOL, the other from SIXTRK, which is used in SPS experiment studies. The results agree very well. This could provide evidence that E778 and the experiment on SPS are comparable.

Based on these tracking results, there are at least two explanations for the experimental value that can be drawn. First, the reason that the measured value is smaller might be the two-degree motion in the real machine. Figure 35 shows the difference between 1-D and 2-D motion. But this difference is a little bit too small to explain the measured value. The other reason might be the effect of tune modulation. From Figure 34, it can be found that if the tune modulation with amplitude of 0.005 is included,

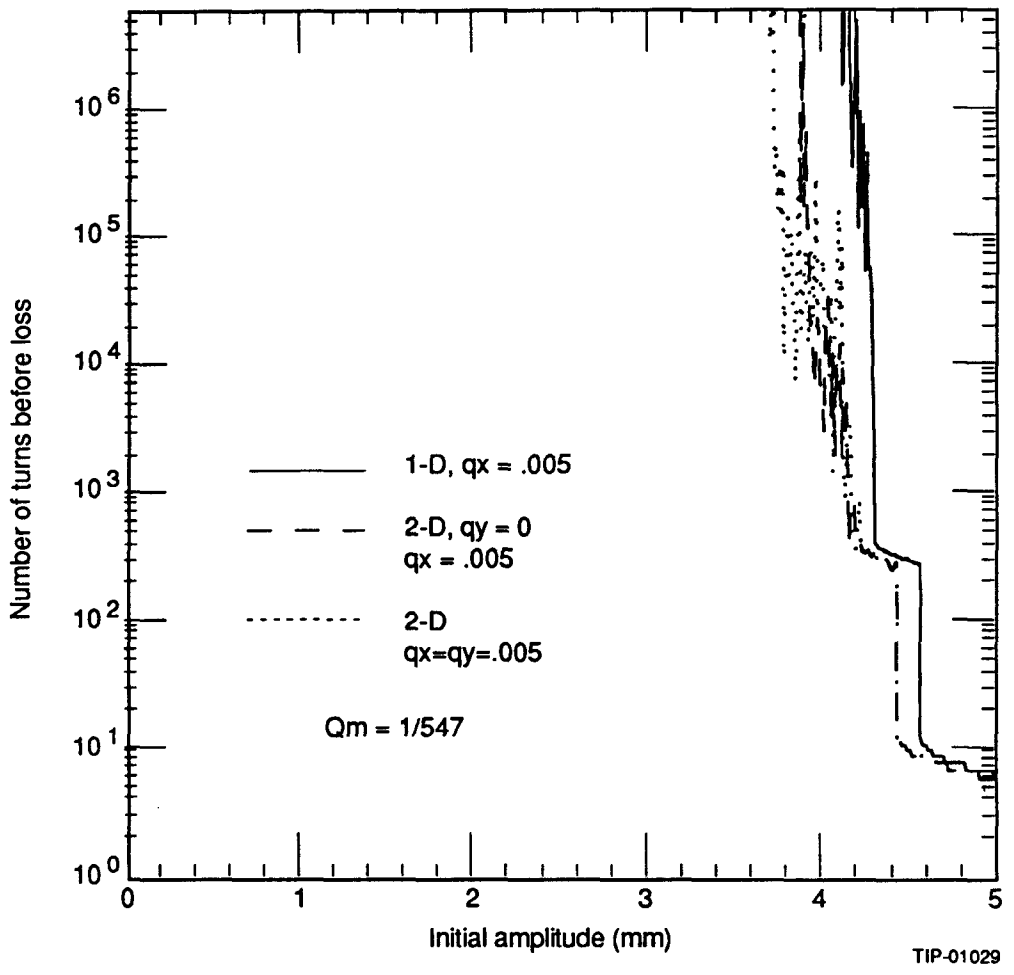

Figure 36. Dynamic Aperture of Two-Dimension Motion with Tune Modulation.

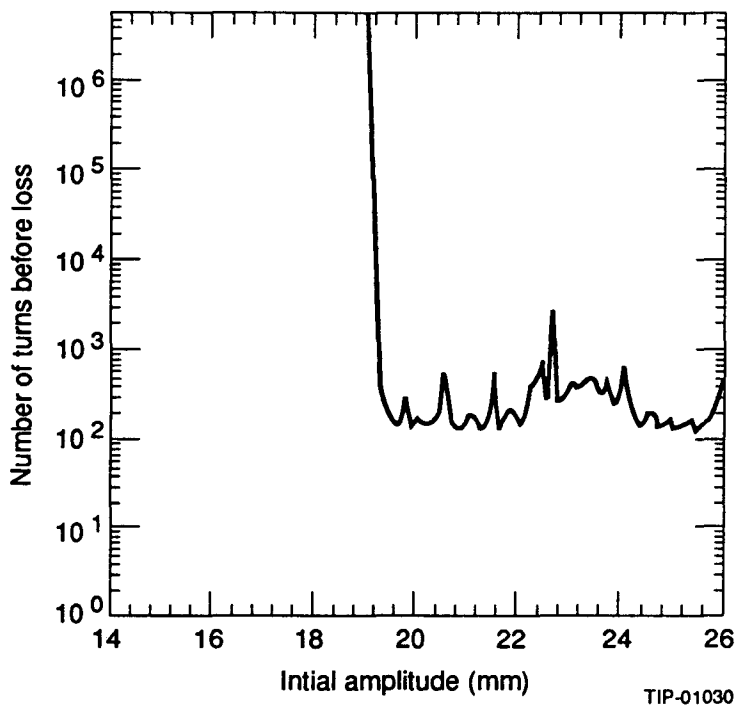

Figure 37. Dynamic Aperture Calculation of SPS for Comparing Different Code (EVOL).

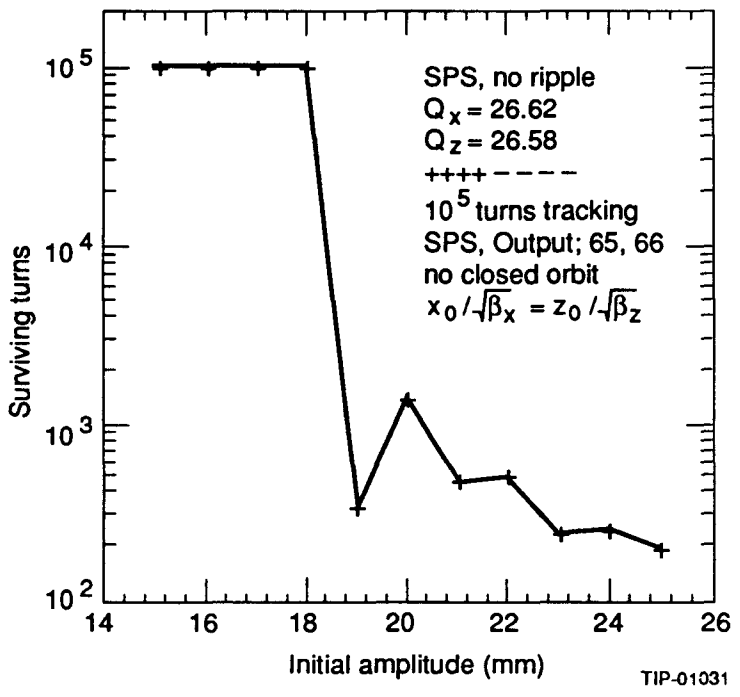

Figure 38. Dynamic Aperture Calculation of SPS for Comparing Different Code (SIXTRACK).

the computed dynamic aperture agrees with the experimental value, 10 mm. It is hard to find out the exact value of tune modulation amplitude in the experiment; however, 0.005 is not a ridiculous value.

The reason that the dynamic aperture is reduced by tune modulation is being studied. At dynamic aperture, the amplitude is too large to compute the nonlinear behavior by perturbation method. The amplitude-dependent tune will not follow quadratic curve at large amplitude, dropping (or rising) much faster. Usually, dynamic aperture appears where the slope of the tune shift versus amplitude curve becomes very large. At that point, the phase advance, or the tune, is extremely sensitive to the amplitude. Any little nonlinear force, like resonance-driven perturbation, will drive the particle out of tuning, and losing it quickly. So, it is assumed that a critical slope of the tune shift versus amplitude curve determines dynamic aperture.

The tune shift versus amplitude curve depends not only on the nonlinear field, but also on the basic tune. A small change of basic tune may cause significant change of the tune shift versus amplitude curve. The critical curve slope will appear at different amplitude, so that the dynamic aperture changes. Figure 39 shows the detuning curve with different basic tunes. The curves end at dynamic aperture.

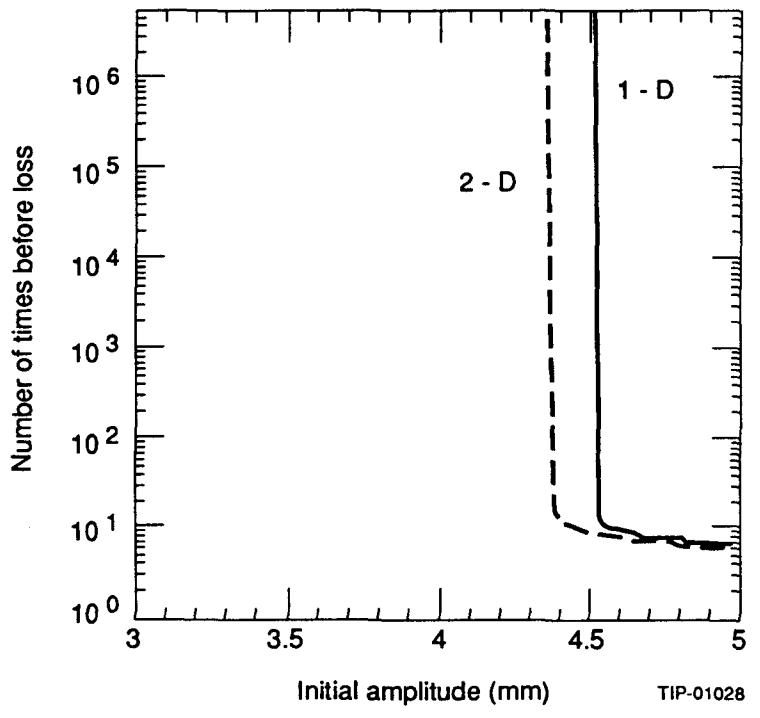

Figure 39. Tune vs. Amplitude with Different Basic Tunes.

Actually, tune modulation changes basic tune continuously. Sometimes, the tune change makes dynamic aperture smaller than original dynamic aperture, i.e., without any tune modulation. Ignoring the time dependence, the particles between the original dynamic aperture and the smallest dynamic aperture achieved when tune modulation reaches its peak

value will get lost eventually. Note that in Figure 34, with tune modulation, most particles are lost within one tune modulation period.

In Figure 39, the dashed line and the dotted line have tune shifts of 0.001 and 0.005, respectively, with respect to the solid line case. The tune shifts have the same value of the tune modulation depth in Figure 34. Comparing Figures 34 and 39, one concludes that detuning curves stop at the amplitudes in corresponding cases. In other words, dynamic aperture with tune modulation is about the same as dynamic aperture without tune modulation, but basic tune changes as much as the tune modulation amplitude in the direction of making the dynamic aperture smaller.

This might explain the 28% smaller experimental result. It also suggests that the effect of tune modulation on dynamic aperture can be estimated by calculating dynamic aperture with basic tune shifted by the amount of projected tune modulation amplitude. To confirm the analysis, more investigation is needed on this subject. I suggest that the dynamic aperture be measured with intentional tune modulation in the next run, and the results compared with Figure 34. More understanding on the effect of tune modulation might be found. More tracking is also necessary to provide evidence. Two-degree dynamic aperture measurement could be included on the E778 agenda.

ACKNOWLEDGEMENTS

Thanks are due to all the members of the E778 collaboration and to others for the direct and indirect contributions they have made to this paper. Most work was done with Steve Peggs or under his guidance. George Tsironis contributed much to driven pendulum theory. And there were many helpful discussions with A. Chao and R. Talman. Sincere thanks to all of them.